https://doi.org/10.5194/egusphere-2026-2125
Preprint. Discussion started: 5 June 2026

Implementation and evaluation of the lognormal prior probability distribution in a variational atmospheric inversion framework

Martin Vojta[1,2,*], Rona L. Thompson[3,*], and Ignacio Pisso[3]

[1]Department of Meteorology and Geophysics, University of Vienna, Vienna, Austria
[2]Department of Chemistry, Environmental Chemical Processes Laboratory (ECPL), University of Crete, Crete, Greece
[3]NILU, Kjeller, Norway
[*]These authors contributed equally to this work.

Correspondence: Martin Vojta (martin.vojta@univie.ac.at)

Abstract.

In this study, we investigate the use of a lognormal prior probability distribution in atmospheric inverse modelling. We present the formal implementation in a variational inversion framework and analyze how the choice of statistical optimization parameter (mean, median, or mode) affects the inversion outcome. Using a case study of inverse modelling of sulfur hexafluoride (SF_6) in Europe, we evaluate the performance of the lognormal implementation through both synthetic and real data experiments, and compare the results to inversions using a normal prior probability distribution. We estimate the posterior uncertainties using a Monte Carlo approach and examine their distribution.

We find that optimizing for the mean or the mode can produce improved emission estimates under the condition of a strong observational constraint, however, this can lead to unstable and strongly biased inversion results under a weak constraint. In contrast, optimizing for the median consistently improves emission estimates and leads to physically plausible results across all tested cases, providing the most reliable option.

We show that inversions using a lognormal prior distribution produce a similar posterior emission pattern as when using a normal prior distribution, however, avoid non-physical negative emission values and occasionally allow for stronger positive emission adjustments. Posterior uncertainties can be estimated using interpercentile ranges from an ensemble of inversions with prior emission errors following a lognormal distribution. Due to the strong asymmetry of posterior distributions with respect to the sign of the inversion increments, error reduction is better assessed in log space, where it provides a clearer measure of the constraints imposed by the observations.

1 Introduction

Atmospheric inversion is a method to estimate the flux of some atmospheric component, such as a trace gas or an aerosol, based on its measurement in the atmosphere. The methodology combines a prior estimate of the fluxes and a model of atmospheric transport (and depending on the component, also a model of its chemistry or deposition) to relate the fluxes to atmospheric concentrations (or mole fractions). An updated estimate of the fluxes can be found by comparing the modelled and observed concentrations (or mole fractions) and relating this to a correction to be made to the fluxes by effectively inverting the model

https://doi.org/10.5194/egusphere-2026-2125
Preprint. Discussion started: 5 June 2026

relationship, hence the name "atmospheric inversion". Atmospheric inversions have been applied to determining the fluxes of various greenhouse gases since the late 1980s (e.g. Rayner et al., 1999; Tans et al., 1989; Prinn et al., 1990) and more recently for aerosols species (e.g. Evangeliou et al., 2018). The method has become increasingly employed to better quantify fluxes of greenhouse gases to improve understanding of their variation, especially due to climate (e.g. Thompson et al., 2014; Rödenbeck et al., 2018; Peng et al., 2022), as well as to support the quantification of anthropogenic emissions (e.g. Henne et al., 2016; Manning et al., 2011, 2022).

The inversion method was first adopted in seismology and described in detail by Tarantola (2005). It is based in statistical optimization and most commonly is derived from Bayes' Theorem. According to Bayes' Theorem, the posterior probability for some variable, $\mathbf{x}$, given some observations, $\mathbf{y}$, is equivalent to the conditional probability, $P(\mathbf{x} \mid \mathbf{y})$, which is equal to

$$P(\mathbf{x} \mid \mathbf{y}) = \frac{P(\mathbf{x})P(\mathbf{y} \mid \mathbf{x})}{P(\mathbf{y})}, \tag{1}$$

where $P(\mathbf{x})$ is the probability for the prior estimate of $\mathbf{x}$, $P(\mathbf{y} \mid \mathbf{x})$ is the conditional probability (i.e., the probability of observing $\mathbf{y}$ given $\mathbf{x}$), and $P(\mathbf{y})$ is the marginal probability of the observation (Rodgers, 2000, e.g.). Since $P(\mathbf{y})$ is constant, $P(\mathbf{x} \mid \mathbf{y})$ is proportional only to $P(\mathbf{x})$ and $P(\mathbf{y} \mid \mathbf{x})$.

Atmospheric inversion aims to find the most probable solution for $\mathbf{x}$, that is, the fluxes, based on atmospheric observations, $\mathbf{y}$. The fluxes discretized in 2D space can be described by a vector, $\mathbf{x}$, often referred to as the state vector, and the observations can be described by a vector, $\mathbf{y}$, the observation vector. The atmospheric model that relates the state variables to the observations can be described by an operator, $\mathcal{H}$, that maps from the state to the observation space.

The application of Bayes' theorem for inverse modelling requires the formulation of probability density functions (PDFs) to describe variables being analysed. Since the error distribution of these variables is usually unknown they are typically assumed to follow a normal (Gaussian) distribution, as this simplifies the mathematical implementation. Gaussian distributions have a big advantage that the combination (i.e. product) of two normalized Gaussian PDFs results in another Gaussian distribution, allowing for an easy formalism of Eq. 1 yielding a Gaussian posterior probability distribution $P(\mathbf{x} \mid \mathbf{y})$. This posterior probability distribution can be characterized by its mean and standard deviation, which both can be determined analytically.

However, a lognormal distribution is common in nature and thus in real data (Limpert et al., 2001). The prior emission estimates for many atmospheric species have a lognormal distribution, strongly suggesting that the errors follow a lognormal distribution as well. A variable $\mathbf{x}$ is lognormally distributed when $\ln(\mathbf{x})$ is normally distributed. Unlike the normal distribution for which the mean, median, and mode are the same value, in the lognormal distribution $\mathbf{x}_{\text{mode}} < \mathbf{x}_{\text{median}} < \mathbf{x}_{\text{mean}}$ and thus we need to choose which parameter we use to derive the cost function. Furthermore, the long tail of the lognormal distribution accounts for the possibility of large errors, for which the probability is vanishingly small under a normal distribution. Another appeal of the lognormal distribution for the prior, is that it is only defined for positive values of $\mathbf{x}$, thus it ensures a positive posterior solution, which is not the case with a normal distribution. This is particularly useful when negative fluxes are non-physical, or in the case that one wishes to preserve the sign of the prior state variables, which is possible when $\ln(\mathbf{x})$ represents scalars of the prior state variables.

https://doi.org/10.5194/egusphere-2026-2125
Preprint. Discussion started: 5 June 2026

In atmospheric inversions, there are a few examples where a lognormal distribution has been used to describe probability distribution of the prior and, in some cases also the observations (e.g., Brioude et al., 2011; Ganesan et al., 2014; Zammit-Mangion et al., 2016; Chen et al., 2023). However, to our knowledge, there has not yet been a thorough examination of the performance of atmospheric inversions using a lognormal prior uncertainty distribution, specifically regarding the choice of statistical parameter and the PDF of the posterior uncertainty. In this study, we present the derivation of the cost functions for lognormal prior probability and the gradients of the cost functions as needed in a variational inversion framework. We further discuss the performance of the lognormal-based inversion through both synthetic and real data experiments using a case study of European SF_6 inversions. Finally, we compare the results to inversions using a normal prior distribution, and discuss the estimation of posterior uncertainties using a Monte Carlo approach.

2 Methodology

2.1 Derivation of the cost function

In this study, we consider a lognormal distribution for the prior probability. For a state vector $\mathbf{x}$ of dimension N, the PDF f_X of a multivariate lognormal distribution is

$$f_X(\mathbf{x}) = \frac{1}{(2\pi)^{N/2}|\boldsymbol{\Sigma}|^{1/2}} \left(\prod_{i=1}^{N} \frac{1}{x_i}\right) \exp\left(-\frac{1}{2}(\ln(\mathbf{x}) - \boldsymbol{\mu})^\top \boldsymbol{\Sigma}^{-1}(\ln(\mathbf{x}) - \boldsymbol{\mu})\right), \tag{2}$$

defined for strictly positive values of all components of $\mathbf{x}$, where $\boldsymbol{\mu}$ and $\boldsymbol{\Sigma}$ represent the mean and the covariance of the normally distributed variable, $\ln(\mathbf{x})$. The median, mean, and mode of the lognormal distribution can be expressed in terms of $\boldsymbol{\mu}$ and $\boldsymbol{\Sigma}$ as:

$$\mathbf{x}_{\text{median}} = \exp(\boldsymbol{\mu}), \tag{3}$$

$$\mathbf{x}_{\text{mean}} = \exp(\boldsymbol{\mu} + \frac{1}{2}\text{diag}(\boldsymbol{\Sigma})), \tag{4}$$

$$\mathbf{x}_{\text{mode}} = \exp(\boldsymbol{\mu} - \text{diag}(\boldsymbol{\Sigma})). \tag{5}$$

The errors $\boldsymbol{\varepsilon}$ for the lognormal distribution are geometric, meaning that they are defined as multiplicative factors relative to the prior estimate $\mathbf{x}_b$, rather than additive constants (Cohn, 1997; Fletcher and Zupanski, 2006).

$$\mathbf{x} = \mathbf{x}_b\,\boldsymbol{\varepsilon} \quad \Longrightarrow \quad \ln\boldsymbol{\varepsilon} = \ln\mathbf{x} - \ln\mathbf{x}_b. \tag{6}$$

https://doi.org/10.5194/egusphere-2026-2125
Preprint. Discussion started: 5 June 2026

The transformed PDF (Eq. 2) in terms of the error $\boldsymbol{\varepsilon}$ reads:

$$P(\boldsymbol{\varepsilon}) = \frac{1}{(2\pi)^{N/2}|\boldsymbol{\Sigma}|^{1/2}} \left(\prod_{i=1}^{N} \frac{1}{\varepsilon_i}\right) \exp\left(-\frac{1}{2}\ln(\boldsymbol{\varepsilon})^{\top}\boldsymbol{\Sigma}^{-1}\ln(\boldsymbol{\varepsilon})\right), \tag{7}$$

where the mean of $\ln\boldsymbol{\varepsilon}$ is zero, corresponding to an unbiased distribution required for the optimization.

The conditional probability, $P(\mathbf{y} \mid \mathbf{x})$, provides the connection between the state, $\mathbf{x}$, and the observation, $\mathbf{y}$. Following Lorenc (1986), $P(\mathbf{y} \mid \mathbf{x})$ can be expressed in terms of the observation-error probability density function $P_o(\mathbf{y} - \mathbf{y}_{\text{mod}})$ when the assumed error distribution is defined over the entire real line, such as in the Gaussian case. Here, $\mathbf{y}_{\text{mod}}$ (representing the modeled observations) depends on $\mathbf{x}$ according to:

$$\mathbf{y}_{\text{mod}} = \mathcal{H}(\mathbf{x}), \tag{8}$$

where $\mathcal{H}$ is an operator, such as an atmospheric model, that maps from the state to the observation space.

The observation-error probability density function $P_o(\mathbf{y} - \mathbf{y}_{\text{mod}})$ is assumed to be Gaussian

$$P_o(\mathbf{y} - \mathbf{y}_{\text{mod}}) \propto \exp\left(-\frac{1}{2}(\mathbf{y} - \mathcal{H}(\mathbf{x}))^{\top}\mathbf{R}^{-1}(\mathbf{y} - \mathcal{H}(\mathbf{x}))\right), \tag{9}$$

where $\mathbf{R}$ is the error covariance matrix in the observation space, which includes the observation error as well as errors associated with the operator $\mathcal{H}$.

The maximum a posterior (MAP) solution for $\boldsymbol{\varepsilon}$ is equivalent to minimizing the function $-\ln(P(\boldsymbol{\varepsilon} \mid \mathbf{y}))$, which can be found by inserting the definitions of $P(\boldsymbol{\varepsilon})$ and $P_o(\mathbf{y} - \mathbf{y}_{\text{mod}})$ into Eq. 1 and taking the logarithm

$$-\ln(P(\boldsymbol{\varepsilon} \mid \mathbf{y})) \propto -\ln\left(\prod_{i=1}^{N} \frac{1}{\varepsilon_i}\right) + \frac{1}{2}(\ln(\boldsymbol{\varepsilon}))^{\top}\boldsymbol{\Sigma}^{-1}\ln(\boldsymbol{\varepsilon}) + \frac{1}{2}(\mathcal{H}(\mathbf{x}) - \mathbf{y})^{\top}\mathbf{R}^{-1}(\mathcal{H}(\mathbf{x}) - \mathbf{y}). \tag{10}$$

From Eq. 10, we derive the cost function for the MAP solution, which is equivalent to finding the mode solution of the posterior PDF. This can be written as

$$J_{\text{mod}}(\mathbf{x}) = (\ln(\mathbf{x}/\mathbf{x}_b))^{\top}\mathbf{1} + \frac{1}{2}(\ln(\mathbf{x}) - \ln(\mathbf{x}_b))^{\top}\boldsymbol{\Sigma}^{-1}(\ln(\mathbf{x}) - \ln(\mathbf{x}_b)) + \frac{1}{2}(\mathcal{H}(\mathbf{x}) - \mathbf{y})^{\top}\mathbf{R}^{-1}(\mathcal{H}(\mathbf{x}) - \mathbf{y}), \tag{11}$$

where $\mathbf{1}$ is a vector of ones with the same length as $\mathbf{x}$, and using the fact that $\ln(\boldsymbol{\varepsilon}) = \ln(\mathbf{x}) - \ln(\mathbf{x}_b)$.

Unlike the normal PDF, the mode, median, and mean of the lognormal distribution differ and thus there are different cost functions for each parameter.

Fletcher and Zupanski (2006) provide modified cost functions for the mean and median of the univariate lognormal distribution. Adapting these expressions to the prior in the present multidimensional case, we obtain for the median:

$$J_{\text{med}}(\mathbf{x}) = \frac{1}{2}(\ln(\mathbf{x}) - \ln(\mathbf{x}_b))^{\top}\boldsymbol{\Sigma}^{-1}(\ln(\mathbf{x}) - \ln(\mathbf{x}_b)) + \frac{1}{2}(\mathcal{H}(\mathbf{x}) - \mathbf{y})^{\top}\mathbf{R}^{-1}(\mathcal{H}(\mathbf{x}) - \mathbf{y}), \tag{12}$$

,

https://doi.org/10.5194/egusphere-2026-2125
Preprint. Discussion started: 5 June 2026

while the cost function[1] for the mean is:

$$J_{\text{mean}}(\mathbf{x}) = -\frac{1}{2}\left(\ln(\mathbf{x}/\mathbf{x}_b)\right)^\top \mathbf{1} + \frac{1}{2}\left(\ln(\mathbf{x}) - \ln(\mathbf{x}_b)\right)^\top \mathbf{\Sigma}^{-1}\left(\ln(\mathbf{x}) - \ln(\mathbf{x}_b)\right) + \frac{1}{2}\left(\mathcal{H}(\mathbf{x}) - \mathbf{y}\right)^\top \mathbf{R}^{-1}\left(\mathcal{H}(\mathbf{x}) - \mathbf{y}\right). \tag{13}$$

The question of which parameter, and thus which cost function, to choose for the optimization has been discussed by Fletcher and Zupanski (2006) in the context of data assimilation. The decision is based on considering the values for the median, mean, and mode of the lognormal distribution (Eqs. 3,4 and 5). The mean increases without bound as the variance grows, making it less suitable for data assimilation. In contrast, the median remains independent of the variance, while the mode is the only parameter that is bounded with respect to the variance and explicitly depends on the covariance structure (Fletcher and Zupanski, 2006). However, subsequent studies (e.g. Fletcher et al., 2019) showed that there are regions where each one of these three parameters are optimal at minimizing the errors. Specifically, if the background term $\mathbf{x}_b$ is close to the true state then the median emerges as the best estimator.

2.2 Implementation in a variational inversion framework

First, we describe the implementation for the mode solution. For simplicity, we use the substitution $\mathbf{z} = \ln(\mathbf{x}/\mathbf{x}_b)$ to give:

$$J_{\text{mod}}(\mathbf{z}) = \mathbf{z}^T\mathbf{1} + \frac{1}{2}\mathbf{z}^T\mathbf{\Sigma}^{-1}\mathbf{z} + \frac{1}{2}\big(\mathcal{H}(\mathbf{x}_b\exp(\mathbf{z})) - \mathbf{y}\big)^T\mathbf{R}^{-1}\big(\mathcal{H}(\mathbf{x}_b\exp(\mathbf{z})) - \mathbf{y}\big). \tag{14}$$

It is important to note that the posterior state variables, $\mathbf{x}$, will always be of the same sign as the prior, $\mathbf{x}_b$, because $\mathbf{z} \leq 0$ is undefined. This is a very useful property because it means that variables that can physically only have positive values will remain positive a posteriori. On the other hand, if some of the variables in $\mathbf{x}_b$ are negative, these will remain negative a posteriori.

When the transport function $\mathcal{H}(\mathbf{x})$ is linear, as is commonly the case for Lagrangian models, it can be expressed as a matrix operator $\mathbf{H}$. In that case the gradient of the cost function reads:

$$J'_{\text{mod}}(\mathbf{z}) = \mathbf{1} + \mathbf{\Sigma}^{-1}\mathbf{z} + \text{diag}(\mathbf{x}_b\exp(\mathbf{z}))\mathbf{H}^T\mathbf{R}^{-1}\big(\mathbf{H}(\mathbf{x}_b\exp(\mathbf{z})) - \mathbf{y}\big). \tag{15}$$

Here we used that $\mathcal{H}^* := \left(\frac{\partial\mathcal{H}}{\partial\mathbf{x}}\right)^T$ reduces to $\mathbf{H}^T$ for a linear operator, with T denoting the matrix transpose. In the general nonlinear case, the formal expression of the gradient is the same, but we keep $\mathcal{H}^*$ to denote the adjoint of $\mathcal{H}$ instead of writing it as a matrix transpose.

Analogous to the pre-conditioning done for a normal PDF, the variable $\mathbf{z}$ can be substituted for $\boldsymbol{\chi}$, where $\boldsymbol{\chi} = \mathbf{\Sigma}^{-1/2}\mathbf{z}$, to improve the convergence rate. Substituting $\boldsymbol{\chi}$ into Eq. 14 gives:

[1]These expressions for the cost functions correspond to the univariate lognormal case, consistent with our prior distribution. Our posterior distribution, however, is a Gaussian–lognormal posterior (GLP), resulting from combining a Gaussian likelihood with a lognormal prior. Although the posterior does not generally have a closed-form expression, these cost functions provide the approximations for the respective posterior parameters.

https://doi.org/10.5194/egusphere-2026-2125
Preprint. Discussion started: 5 June 2026

$$J_{\text{mod}}(\boldsymbol{\chi}) = (\boldsymbol{\Sigma}^{1/2}\boldsymbol{\chi})^T\mathbf{1} + \frac{1}{2}\boldsymbol{\chi}^T\boldsymbol{\chi} + \frac{1}{2}\big(\mathbf{H}(\mathbf{x}_b\exp(\boldsymbol{\Sigma}^{1/2}\boldsymbol{\chi})) - \mathbf{y}\big)^T\mathbf{R}^{-1}\big(\mathbf{H}(\mathbf{x}_b\exp(\boldsymbol{\Sigma}^{1/2}\boldsymbol{\chi})) - \mathbf{y}\big) \tag{16}$$

and the gradient of Eq. 16 is:

$$J'_{\text{mod}}(\boldsymbol{\chi}) = \boldsymbol{\Sigma}^{1/2}\mathbf{1} + \boldsymbol{\chi} + \boldsymbol{\Sigma}^{1/2}\text{diag}\big(\mathbf{x}_b\exp(\boldsymbol{\Sigma}^{1/2}\boldsymbol{\chi})\big)\mathbf{H}^T\mathbf{R}^{-1}\big(\mathbf{H}(\mathbf{x}_b\exp(\boldsymbol{\Sigma}^{1/2}\boldsymbol{\chi})) - \mathbf{y}\big). \tag{17}$$

The $\mathbf{z}$ for which Eq. 14 is at a minimum is found by solving $J'_{\text{mod}}(\boldsymbol{\chi}) = 0$.

For the median solution, we derive the expression for the gradient of the cost function in Eq. 12, which is:

$$J'_{\text{med}}(\mathbf{z}) = \boldsymbol{\Sigma}^{-1}\mathbf{z} + \text{diag}(\mathbf{x}_b\exp(\mathbf{z}))\mathbf{H}^T\mathbf{R}^{-1}\big(\mathbf{H}(\mathbf{x}_b\exp(\mathbf{z})) - \mathbf{y}\big). \tag{18}$$

By applying the pre-conditioning and substituting $\boldsymbol{\chi}$ into Eq.12, we get the cost function for $\boldsymbol{\chi}$:

$$J_{\text{med}}(\boldsymbol{\chi}) = \frac{1}{2}\boldsymbol{\chi}^T\boldsymbol{\chi} + \frac{1}{2}\big(\mathbf{H}(\mathbf{x}_b\exp(\boldsymbol{\Sigma}^{1/2}\boldsymbol{\chi})) - \mathbf{y}\big)^T\mathbf{R}^{-1}\big(\mathbf{H}(\mathbf{x}_b\exp(\boldsymbol{\Sigma}^{1/2}\boldsymbol{\chi})) - \mathbf{y}\big) \tag{19}$$

and the gradient of Eq. 19 is:

$$J'_{\text{med}}(\boldsymbol{\chi}) = \boldsymbol{\chi} + \boldsymbol{\Sigma}^{1/2}\text{diag}\big(\mathbf{x}_b\exp(\boldsymbol{\Sigma}^{1/2}\boldsymbol{\chi})\big)\mathbf{H}^T\mathbf{R}^{-1}\big(\mathbf{H}(\mathbf{x}_b\exp(\boldsymbol{\Sigma}^{1/2}\boldsymbol{\chi})) - \mathbf{y}\big). \tag{20}$$

For the mean optimization, we derive the expression for the gradient of the cost function in Eq. 13, which is

$$J'_{\text{mean}}(\mathbf{z}) = -\frac{1}{2}\mathbf{1} + \boldsymbol{\Sigma}^{-1}\mathbf{z} + \text{diag}(\mathbf{x}_b\exp(\mathbf{z}))\mathbf{H}^T\mathbf{R}^{-1}\big(\mathbf{H}(\mathbf{x}_b\exp(\mathbf{z})) - \mathbf{y}\big). \tag{21}$$

By again applying the pre-conditioning and substituting $\boldsymbol{\chi}$ into Eq.13, we get the cost function for $\boldsymbol{\chi}$

$$J_{\text{mean}}(\boldsymbol{\chi}) = -\frac{1}{2}(\boldsymbol{\Sigma}^{1/2}\boldsymbol{\chi})^T\mathbf{1} + \frac{1}{2}\boldsymbol{\chi}^T\boldsymbol{\chi} + \frac{1}{2}\big(\mathbf{H}(\mathbf{x}_b\exp(\boldsymbol{\Sigma}^{1/2}\boldsymbol{\chi})) - \mathbf{y}\big)^T\mathbf{R}^{-1}\big(\mathbf{H}(\mathbf{x}_b\exp(\boldsymbol{\Sigma}^{1/2}\boldsymbol{\chi})) - \mathbf{y}\big) \tag{22}$$

and the gradient of Eq. 22 is

$$J'_{\text{mean}}(\boldsymbol{\chi}) = -\frac{1}{2}\boldsymbol{\Sigma}^{1/2}\mathbf{1} + \boldsymbol{\chi} + \boldsymbol{\Sigma}^{1/2}\text{diag}\big(\mathbf{x}_b\exp(\boldsymbol{\Sigma}^{1/2}\boldsymbol{\chi})\big)\mathbf{H}^T\mathbf{R}^{-1}\big(\mathbf{H}(\mathbf{x}_b\exp(\boldsymbol{\Sigma}^{1/2}\boldsymbol{\chi})) - \mathbf{y}\big). \tag{23}$$

Equations 16 and 17 for the mode, Eqs. 19 and 20 for the median, and Eqs. 22 and 23 for the mean solution, are the key expressions needed for the implementation in the variational inversion framework, where a solution is obtained by iteratively adjusting the state vector in the direction of steepest descent, i.e. opposite to the gradient of the cost function.

https://doi.org/10.5194/egusphere-2026-2125
Preprint. Discussion started: 5 June 2026

2.3 Uncertainty in the state space

In inverse modelling, prior emission uncertainties $\boldsymbol{\sigma}_b$ are often estimated as fraction $\boldsymbol{\sigma}$ of the corresponding prior emission values $\mathbf{x}_b$ in each grid cell:

$$\boldsymbol{\sigma}_b = \boldsymbol{\sigma} \cdot \mathbf{x}_b. \tag{24}$$

For the lognormal implementation in the state space, the error covariance matrix, $\boldsymbol{\Sigma}$, needs to describe the uncertainty $\mathbf{s}$ of the log-transformed variable $\mathbf{z}$, which can be expressed in terms of $\boldsymbol{\sigma}$ as:

$$\boldsymbol{s} = \ln(\mathbf{1} + \boldsymbol{\sigma}). \tag{25}$$

Then, the error covariance matrix of $\mathbf{z}$ is:

$$\boldsymbol{\Sigma} = \begin{pmatrix} s_1^2 & c_{12}s_1s_2 & \dots & c_{1N}s_1s_N \\ c_{21}s_2s_1 & s_2^2 & \dots & c_{2N}s_2s_N \\ \vdots & \vdots & \ddots & \vdots \\ c_{N1}s_Ns_1 & c_{N2}s_Ns_2 & \dots & s_N^2 \end{pmatrix}, \tag{26}$$

where c_{ij} represents the correlation between the i-th and j-th element.

3 Evaluation

3.1 Lognormally distributed emission values

To test the performance of the implementation of the lognormal distribution we perform inversions for SF_6 focusing on Europe and the year 2020. SF_6 fluxes are exclusively positive, as land sinks are negligibly small. Figure 1 represents the a priori SF_6 flux distribution in Europe provided by the well-established bottom-up inventories EDGAR (version 8; EDGAR, 2023; Crippa et al., 2023) and GAINS (Purohit and Höglund-Isaksson, 2017), regridded to a spatial resolution of 0.25°. Both inventories exhibit a positively skewed distribution characterized by a large number of small emission values and a long tail extending toward higher values (Fig. 1a/c). This shape is well-approximated by a lognormal distribution. The lognormal shape arises because emission inventories often distribute national totals using proxy data, such as population density, which itself tends to follow a lognormal distribution. Additionally, the assignment of major emissions to specific point sources contributes to the long tail of the distribution. Fig. 1b/d shows the distribution of the logarithm of the emission values, which is well described by a normal PDF for both inventories, making the lognormal nature of the emission distribution apparent. SF_6, therefore, provides a good test case for the lognormal prior distribution implementation, given that the fluxes are only positive and the priors are lognormally distributed.

https://doi.org/10.5194/egusphere-2026-2125
Preprint. Discussion started: 5 June 2026

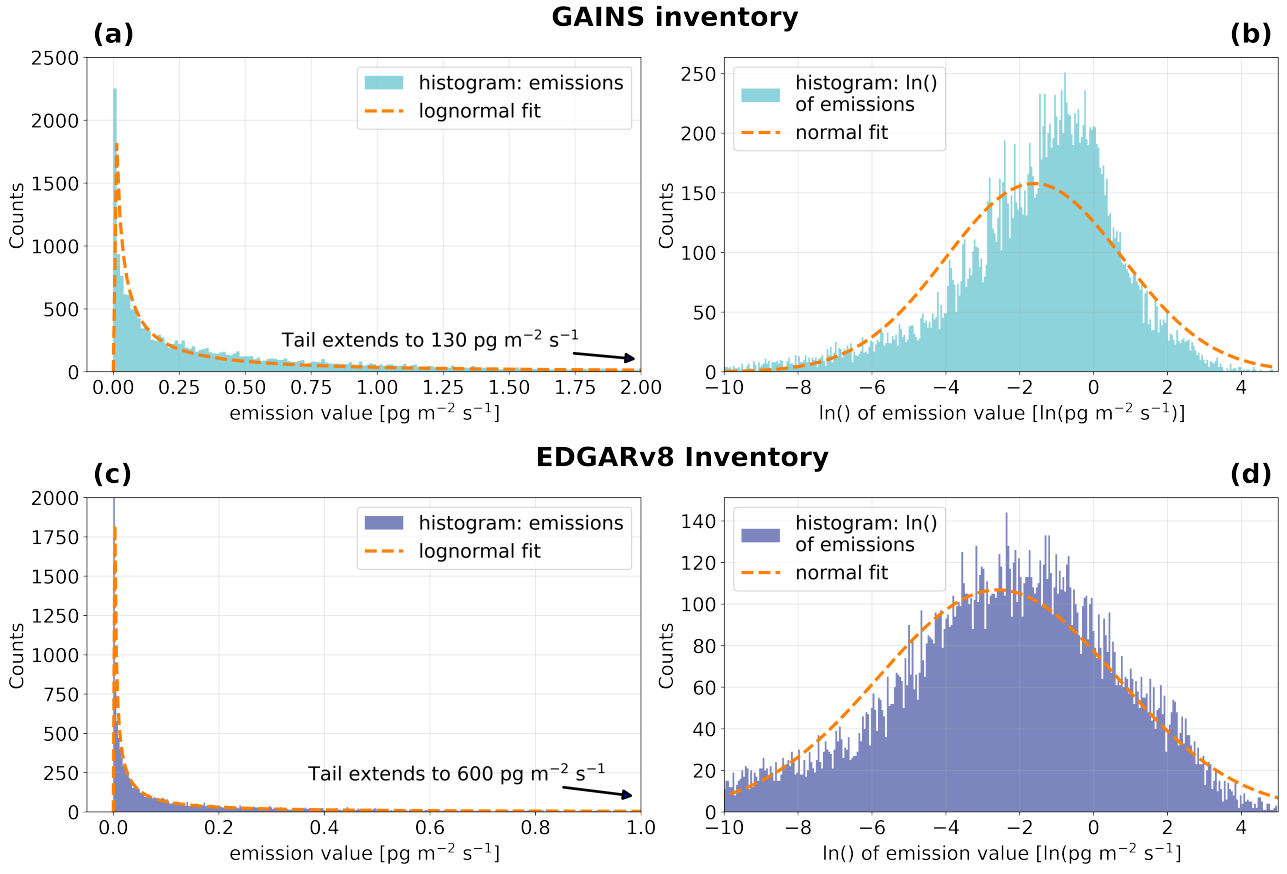

Figure 1. Distribution of the European SF_6 emission. The upper two panels represent the GAINS inventory showing (a) the distribution of the GAINS emission values and (b) the distribution of the logarithm of the GAINS emission values. The lower two panels represent the EDGAR inventory showing (c) the distribution of the EDGAR emission values and (b) the distribution of the logarithm of the EDGAR emission values.

3.2 Inversion Setup

We use the same inversion setup as described in Vojta et al. (2024, 2025), where the methodology is fully described, and provide only a brief overview here.

3.2.1 Observations

In this study, we utilize atmospheric observations of SF_6 dry-air mole fractions from nine European high-frequency surface stations: BSD (Bilsdale), BRM (Beromünster), HFD (Heathfield), JFJ (Jungfraujoch), MHD (Mace Head), RGL (Ridge Hill), TAC (Tacolneston Tall Tower), ZEP (Zeppelin), and ZSF (Zugspitze-Schneefernerhaus). Figure 2 provides an overview of

https://doi.org/10.5194/egusphere-2026-2125
Preprint. Discussion started: 5 June 2026

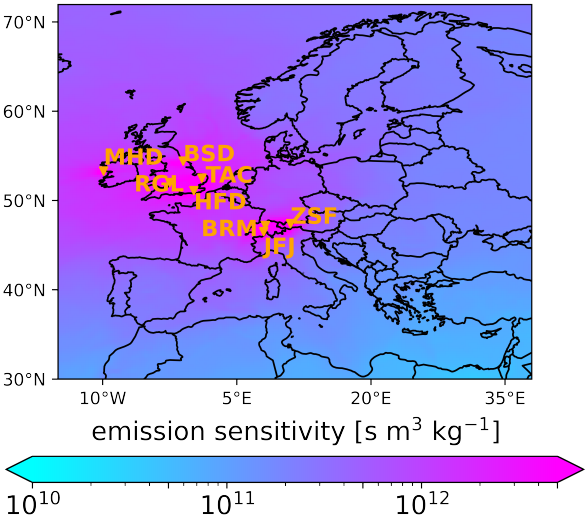

Figure 2. Location of the SF_6 measurement stations and simulated emission sensitivities averaged over 2020.

their locations[2], alongside the modelled emissions sensitivities inside the inversion domain (see Sect 3.2.2). Measurements were averaged over three-hour intervals, and all observations were standardized to the SIO-2005 calibration scale. The used observations are a subset of the dataset created in Vojta et al. (2024), where further details are provided.

3.2.2 Atmospheric transport

To represent the atmospheric transport of SF_6 we utilize the same emission sensitivities that have been calculated in Vojta et al. (2025), where a detailed description can be found. The emission sensitivities characterize how changes in the SF_6 mole fractions are influenced by variations in emissions and are modelled with the Lagrangian particle dispersion model (LPDM) FLEXPART 10.4 (Pisso et al., 2019). For each observation, 50,000 virtual particles are released continuously over a 3-hour period from the measurement site and their trajectories are traced backwards in time for 50 days. The sensitivity of the observation to emissions in a particular grid cell is determined by the average time the particles spend within that cell. Loss processes are neglected, given that SF_6 is almost inert up to the middle stratosphere. Figure 2 displays the emission sensitivities as an average over the year 2020, along with the measurement locations (see Sect. 3.2.1). The highest sensitivities occur near the measurement stations, which are mainly concentrated in Northwestern Europe, particularly in the UK.

3.2.3 Baseline

Baseline mole fractions, representing the contributions to the observations from emissions occurring prior to the FLEXPART simulation period, are calculated using the Global-Distribution-Based (GDB) method (Vojta et al., 2022). In this approach,

[2]ZEP is not shown in Figure 2 given that its location is outside the nested model domain

https://doi.org/10.5194/egusphere-2026-2125
Preprint. Discussion started: 5 June 2026

FLEXPART back-trajectories are used to determine each observation's sensitivity to the mole fractions at the end of the 50-day simulation period. These sensitivities are calculated by dividing the number of trajectories ending in each grid cell by the total number of trajectories, assuming no loss processes. The resulting sensitivities are then multiplied with globally gridded 3D SF_6 mole fraction fields at the end points of the trajectory and integrated across the globe. This so-called "diffusive backward Lagrangian reconstruction" provides a local approximation to the advection-diffusion equation (Legras et al., 2003, 2005). The mole fraction fields used are from Vojta et al. (2024). Finally, emissions occurring during the 50-day FLEXPART simulation but outside the European domain are added to the baseline.

3.2.4 Synthetic emission and observation data

To evaluate the performance of the lognormal distribution implementation, we conduct a synthetic experiment for European SF_6 emissions in the year 2020. We use the European GAINS SF_6 inventory, regridded to a resolution of 0.25°, as a proxy for the "true" emissions. These true emissions are then perturbed with lognormal distributed errors based on the error characteristics of the lognormal-transformed error covariance matrix $\mathbf{\Sigma}$ (see Sect. 2.3) with:

$$\mathbf{x_{perturbed}} = \mathbf{x_{prior}} = \mathbf{x_{true}} \exp(\mathbf{\Sigma}^{1/2}\hat{\boldsymbol{r}}), \tag{27}$$

where $\hat{\boldsymbol{r}}$ is a vector of random numbers with a mean of 0 and a standard deviation of 1. These perturbed emissions are then used as the a priori estimate in the subsequent inversions to assess the performance of the model.

Using the FLEXPART sensitivities, we simulate observations at the measurement stations (see Sect 3.2.1) based on the true emissions. These simulated "true" observations are subsequently perturbed using random errors, which are generated according to the uncertainty characteristics of the observation error covariance matrix $\mathbf{R}$:

$$\mathbf{y_{perturbed}} = \mathbf{y_{true}} + \mathbf{R}^{1/2}\hat{\boldsymbol{r}}. \tag{28}$$

Figure A1a displays the histogram of the emission perturbation factor, $\exp(\mathbf{\Sigma}^{1/2}\hat{\boldsymbol{r}})$, based on an a priori error covariance matrix $\mathbf{\Sigma}$, with an lognormal transformed uncertainty of 0.59 and a spatial correlation lengths of 250 km. Figure A1b presents the histogram of the observation perturbation, $\mathbf{R}^{1/2}\hat{\boldsymbol{r}}$, corresponding to a measurement error of 0.08 ppt. Figure 3a shows the corresponding perturbed emissions, while the spatial distribution of the perturbations (i.e. perturbed emissions - true emissions) is displayed in Fig. 3b. Large positive perturbations are observed in northern Germany, northern Greece, and southern Serbia, while moderately positive values appear in Spain, France, the UK, Ukraine, Sweden, and Poland. Strong negative perturbations are found in southern Germany, Israel, Moscow, and St. Petersburg, with less pronounced negative values in western Austria, Hungary, northern Serbia, and London.

https://doi.org/10.5194/egusphere-2026-2125
Preprint. Discussion started: 5 June 2026

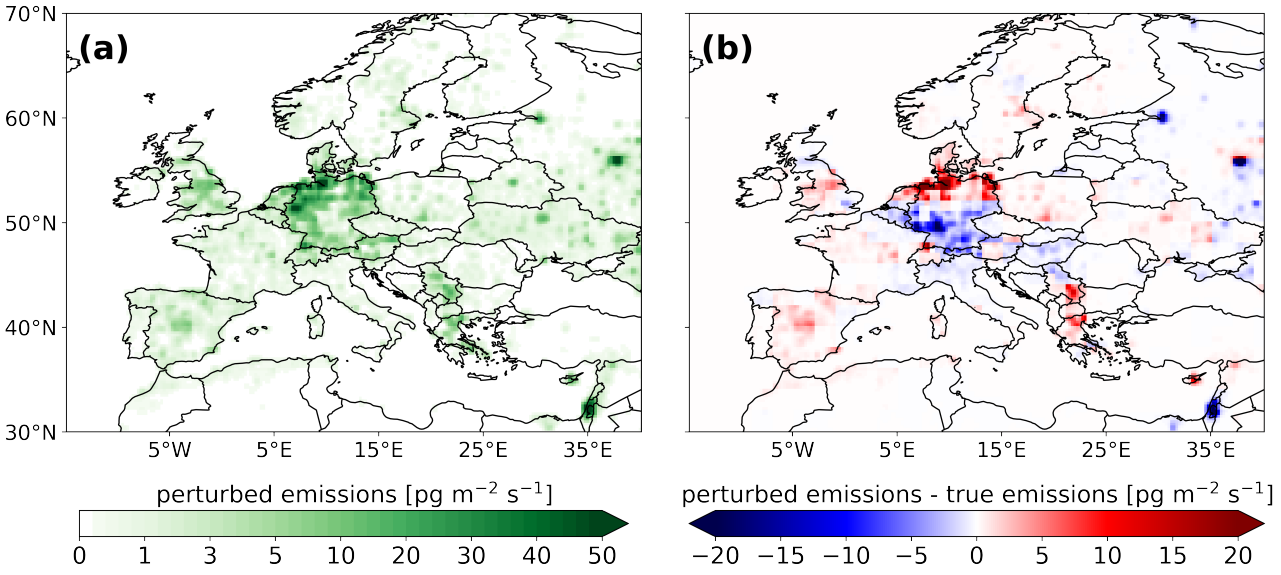

Figure 3. (a) perturbed prior emissions and (b) the spatial distribution of the perturbations (perturbed - true emissions)

3.2.5 Inversion algorithm

We use the Bayesian inversion framework FLEXINVERT+ to find an optimized emission estimate based on the (perturbed) prior emissions and (synthetic) observations (see Sect. 3.2.4/3.2.1), the emission sensitivities (see Sect. 3.2.2) and baseline mole fractions (see Sect. 3.2.3). To minimize the derived cost functions (see Sect. 2.1), we utilize the M1QN3 algorithm (Gilbert and Lemaréchal, 2006), a quasi-Newton method that approximates the inverse Hessian using limited-memory techniques, making it suitable for large-scale minimization problems. For the synthetic data experiment, we limit the algorithm to 40 iterations, as the cost function decreases only slightly beyond this point. For the real-data experiment, we increase the number of iterations to 100 to ensure full convergence. This allows us to rule out the possibility that differences between the posterior emissions obtained using lognormal and normal prior distributions are simply due to incomplete convergence of the cost function. For all performed inversions, we use an emission grid with varying cell sizes ($0.25° \times 0.25°$ - $1.0° \times 1.0°$), determined by aggregating cells with low emission contributions based on emission sensitivities (see Thompson and Stohl, 2014; Vojta et al., 2025). Spatial correlations between emission errors are calculated using an exponential decay function with a correlation length of 250 km, while observation errors are assumed to be uncorrelated. In the inversion, we also optimize baseline mole fractions, where spatially aggregated contributions are optimized in 4 latitude bands, with northern edges at [-30°, 0°, 30°, 90°], using a temporal interval of 28 days, and an uncertainty of 10%.

https://doi.org/10.5194/egusphere-2026-2125
Preprint. Discussion started: 5 June 2026

3.3 Synthetic data experiment setup

To evaluate the performance of the implementation of the lognormal distribution, we perform multiple inversions testing various prior uncertainties of the prior state variables (0.18, 0,34, 0.47, 0.59, 0.69) and observation uncertainties (0.02, 0.04, 0.06, 0.08, 0.1 ppt). Note that prior uncertainty values refer to the log-transformed variable $\mathbf{z}$ and correspond to the relative errors of 0.2, 0.4, 0.6, 0.8, 1.0 in respect to $\mathbf{x}_b$ (see Sect 2.3).

The posterior emissions are evaluated using the Gain metric, G, defined as:

$$G = 1 - \sqrt{\frac{\|\mathbf{x}_{\text{true}} - \mathbf{x}_{\text{post}}\|}{\|\mathbf{x}_{\text{true}} - \mathbf{x}_{\text{prior}}\|}}. \tag{29}$$

G quantifies the improvement achieved through the inversion by comparing the difference between the true and posterior emissions, normalized by the difference between the true and prior emissions. It can range from negative values to 1, with positive values indicating improved performance in approximating the true state relative to the prior estimate, and the higher the value the better the performance.

3.4 Real-data experiment

We perform real-data SF_6 inversions for the year 2020 using the atmospheric observations described in Sect. 3.2.1 and the GAINS inventory as the prior emission estimate. Inversions are conducted with both normal and lognormal prior distributions, and the resulting a posterior emissions are compared. For the lognormal case, the prior uncertainty, defined with respect to the log-transformed variable $\mathbf{z}$ (see Sect. 2.3), is set to 0.41. This corresponds to a relative uncertainty of 50% which is used in the normally distributed case. For both cases the observation error is set to 0.09 ppt.

3.5 A posteriori uncertainty

When using a lognormal prior distribution, the posterior error covariance matrix cannot be derived analytically. To estimate the posterior uncertainties nonetheless, a Monte Carlo approach can be applied, in which the prior emissions are randomly perturbed, and the spread of the resulting posterior emission ensemble is used to derive uncertainty estimates (see e.g., Tarantola, 2005). To test this approach, we construct a 50-member ensemble, where each member is generated by perturbing the prior emissions using lognormally distributed errors, as described by Eq. 27.

We investigate the ensemble error distribution before and after the inversion and assess the departure of the PDF from normality, based on skewness, kurtosis, and the p-value from a normality test, calculated using functions from scipy.stats (skew, kurtosis, normaltest, described in Virtanen et al., 2020). The skewness indicates the asymmetry of a distribution: values near 0 suggest symmetry, positive values indicate a right-skew, and negative values a left-skew. The kurtosis measures tail heaviness: 0 corresponds to a normal distribution, while positive values indicate heavier tails and negative values lighter tails. The normality test (D'Agostino and Pearson, 1973) provides a p-value, with values below 0.05 typically indicating significant

https://doi.org/10.5194/egusphere-2026-2125
Preprint. Discussion started: 5 June 2026

deviation from normality. The relative error reduction is calculated as $1-\frac{\sigma_{\text{post}}}{\sigma_{prior}}$, with σ_{prior} and σ_{post} representing the standard deviations of the prior and posterior ensembles, respectively.

4 Results and discussion

4.1 Synthetic data experiment setup

In the synthetic data experiment we assess how optimizing for the mean, median, or mode affects the quality and stability of the inversion outcome.

4.1.1 Mode

First, we evaluate the implementation of the lognormal prior distribution when optimizing for the mode. Figure 4a presents an overview of the inversion results, showing the Gain metric corresponding to the posterior emissions from 25 inversions, which combine the 5 prior emission uncertainty with the 5 observation uncertainty values (see Sect. 3.3). In many cases, the Gain metric has negative values, indicating that the posterior emissions deviate further from the true emissions compared to the prior emissions. This occurs for cases with a weak observational constraint (i.e. high observation uncertainties) and/or with low prior error. The scenario with the highest observation uncertainty (1.0 ppt) and the lowest prior emission error (0.18) is shown in Fig. 4e and Fig. 4f which illustrate the inversion increments, i.e. posterior minus prior emissions and true minus the prior emissions, respectively. If the inversion performs well, then the pattern of differences should be similar, however, this is not the case. As a consequence of the deterioration of the solution, the discrepancy between the observed and modelled mole fractions increases. To investigate this behavior further, we examine the evolution of the cost with each iteration (Fig. 4b-d). The algorithm minimizes the total cost (Fig. 4b), however, this occurs because the cost in the state space (Fig. 4c) decreases (and becomes negative), while the cost in the observation space (Fig. 4d) increases. This can be explained due to the term $(\ln(\mathbf{x}/\mathbf{x}_b))^\top \mathbf{1}$ in the cost function, which becomes negative when the values of $\mathbf{x}$ fall below their prior estimates $\mathbf{x}_b$ and this drives the solution to lower and lower values for the posterior emissions, $\mathbf{x}$ (see Fig. 4e). This occurs when the observational constraint is weak, i.e., when the term $(\mathbf{H}(\mathbf{x})-\mathbf{y})^T\mathbf{R}^{-1}(\mathbf{H}(\mathbf{x})-\mathbf{y})$ does not have a strong impact on the overall cost. For cases with strong observational constraints, Fig. 4a shows positive Gain metric values, meaning that the posterior approaches the true emissions. For the scenario with the lowest observation uncertainty (0.02 ppt) and the highest a priori emission error (0.69), we see that the total cost decreases (Fig. 4g), primarily due to the cost decrease in the observation space (Fig. 4i), meaning that discrepancy between observed and modelled mole fractions is reduced. Also for this scenario, we see that the cost in the state space becomes negative (Fig. 4h), but this has only a small contribution to the total cost. The negative inversion increments (Fig. 4j) over northern Germany and the UK largely correct the perturbations made to the prior emissions (Fig. 4k) and the positive increments over southern Germany and western Austria partially correct the perturbations in those regions. In other regions, the emission perturbations are not corrected by the inversion, likely due to their small values or the low sensitivity of the observations to these regions.

https://doi.org/10.5194/egusphere-2026-2125
Preprint. Discussion started: 5 June 2026

Mode

$$J_{mod}(\boldsymbol{x}) = \left(\ln(\boldsymbol{x}/\boldsymbol{x_b})\right)^{\mathrm{T}}\mathbf{1} + \frac{1}{2}\left(\ln(\boldsymbol{x}) - \ln(\boldsymbol{x_b})\right)^{\mathrm{T}}\boldsymbol{\Sigma}^{-1}\left(\ln(\boldsymbol{x}) - \ln(\boldsymbol{x_b})\right) + \frac{1}{2}(H(\boldsymbol{x}) - \boldsymbol{y})^{\mathrm{T}}\mathbf{R}^{-1}(H(\boldsymbol{x}) - \boldsymbol{y})$$

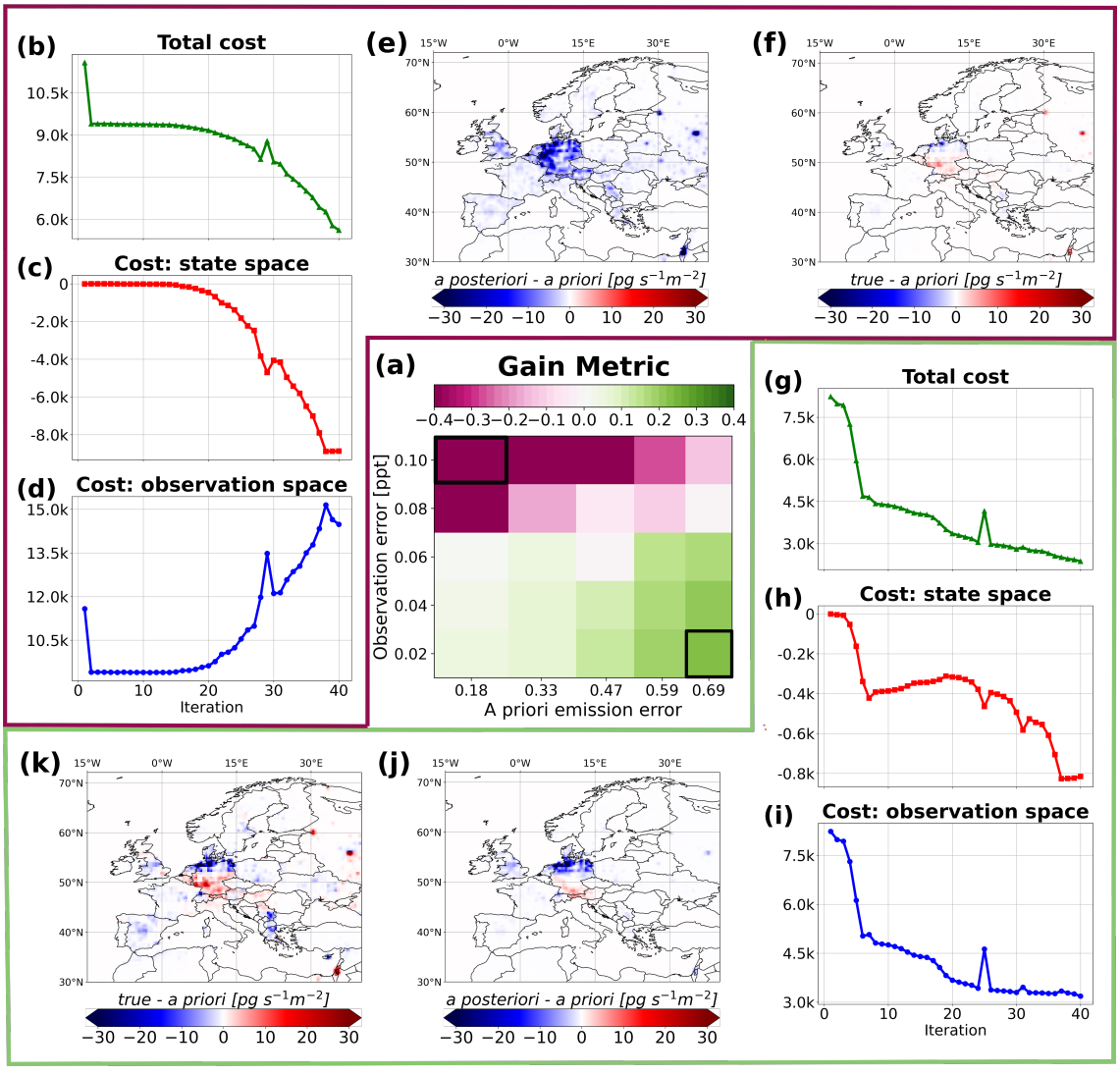

Figure 4. (a) Gain metric for 25 inversions, optimizing for the mode and using different uncertainty settings. Panels (b–d) show the evolution of the total cost (b), state space cost (c), and observation space cost (d) for the case with the weakest observational constraint, while panels (e–f) show the corresponding inversion increments (e) and negative perturbations (f). Panels (g–i) show the evolution of the total (g), state space (h), and observation space (i) cost for the case with the strongest observational constraint, and panels (j–k) show the respective inversion increments (j) and negative perturbations (k).

https://doi.org/10.5194/egusphere-2026-2125
Preprint. Discussion started: 5 June 2026

4.1.2 Mean

Next, we evaluate the implementation of the lognormal prior distribution when optimizing for the mean. Figure 5a presents an overview of the inversion results, showing the Gain metric. In contrast to the mode optimization, Gain metric values are predominantly positive, meaning that the posterior approaches the true emissions in almost all cases. However in the case of inversion configuration with the smallest observational constraint, the Gain metric becomes slightly negative. A closer examination of this case reveals that the total cost (Fig. 5b) decreases, driven by a reduction in the state-space cost (Fig. 5c), while the observation-space cost (Fig. 5d) increases. This results in a greater deviation from the true emission values. This arises from the term $-\frac{1}{2}(\ln(\mathbf{x}/\mathbf{x}_b))^\top \mathbf{1}$ in the cost function, which becomes increasingly negative as the values of $\mathbf{x}$ increase relative to their prior values. As a result, the inversion produces entirely positive emission increments (Fig. 5e), which do not correct the perturbations to the prior emissions (Fig. 5f). In the configuration with the strongest observational constraint, the total cost (Fig. 5g) decreases primarily due to a reduction in the observation-space cost (Fig. 5i). The state-space cost (Fig. 5h) peaks at iteration 14, coinciding with the correction of large-scale patterns in northern Germany, as indicated by the negative increments in Fig.5j. In the following iterations, the optimization targets finer-scale structures, particularly in southern Germany, leading to positive increments and a subsequent decrease in the state-space cost. Generally, the inversion increments (Fig. 5j) are similar to those obtained in the mode-based optimization and largely correct the emission perturbations in Germany (Fig. 5k). Perturbations in the UK are also slightly corrected, although the increment is smaller than in the mode case. This difference is likely due to the fact that optimizing for the mean generally leads to higher posterior emissions, influenced by the term $-\frac{1}{2}(\ln(\mathbf{x}/\mathbf{x}_b))^\top \mathbf{1}$ in the state-space cost function. Please note that the predominantly positive Gain metric values do not necessarily imply that the inversion results are generally better than those from the mode-based optimization. While the observed artifacts appear consistently, the individual Gain values remain strongly influenced by the specific random realization of the emission perturbations and should therefore be interpreted with caution.

4.1.3 Median

Figure 6a presents an overview of the median-based inversion results, showing the Gain metric. In contrast to the mode- and mean-based optimizations, the Gain values are exclusively positive, indicating that in all cases the posterior emissions move closer to the true values. For all configurations, the total cost decreases as emissions deviate from the prior values and thus increasing the state-space cost, while the modelled mole fractions approach the synthetic observations thus decreasing the observation-space cost, as illustrated for the configurations with the weakest (Fig. 6b–d) and strongest (Fig. 6g–i) observational constraints. Overall, inversion performance improves with increasing prior emission uncertainties, as the solution is allowed to deviate more freely from the prior values and becomes more strongly constrained by the observations. In the configuration with the weakest observational constraint, the inversion increments only slightly compensate for some of the negative emission perturbations in southern Germany (Fig. 6e,f). In contrast, stronger observational constraints lead to more accurate corrections of the perturbations (Fig. 6j,k).

https://doi.org/10.5194/egusphere-2026-2125
Preprint. Discussion started: 5 June 2026

4.2 Real data experiment

4.2.1 A posteriori emissions

As a next step, we perform real data inversions, where we use the unperturbed observations (Sec 3.2.1) and the unperturbed GAINS inventory as the prior emission estimate. Figure 7 shows the posterior emissions for (a) normal and (b) lognormal prior probability distributions, while (c) displays the difference between both cases. For the lognormal inversion, we solved for the median solution.

Generally, the posterior emissions are very similar, showing large emissions in southwest Germany and a broadly consistent spatial pattern. However, in the normal distribution case, the algorithm produces small, non-physical negative emissions in northwest Germany (Fig. 7a), which are absent in the lognormal case. In other regions of Germany, Fig. 7c reveals slightly higher posterior emissions in the normal distribution compared to the lognormal case. These elevated emissions may compensate for the negative values in order to match the observed mole fractions and thus could represent an overestimation, which might be avoided by the lognormal distribution. Additionally, around Paris, Fig. 7 shows higher posterior emissions in the lognormal case compared to the normal case, reflecting the larger positive increments obtained in that setup. This difference may result from the long-tailed nature of the lognormal distribution, which allows for larger prior uncertainties. As a consequence, the inversion permits greater positive adjustments to the emissions, potentially leading to higher posterior values in regions where observational constraints support them.

4.2.2 Posterior uncertainty

Finally we estimate the posterior uncertainty, using an 50-member inversion ensemble, in which the prior emissions are perturbed with lognormal errors (see Sect. 3.5). During the inversion process, the lognormal prior distribution is updated using observational data, which are assumed to have normally distributed errors. This transformation to normality is illustrated by Fig. 8 showing (a) changes in the p-value (posterior - prior) , (b) skewness (prior - posterior) and (c) kurtosis (prior - posterior) of the error distribution before and after the inversion. In many grid cells, the posterior distribution becomes more symmetric and transforms towards a Gaussian distribution (green colors), particularly in regions where the observations strongly constrain the emissions.

To illustrate this further, colored dots in Fig. 8a indicate grid cells with the four largest increases in p-values, suggesting significant transformation to normality. The corresponding uncertainty distributions in these locations are examined in detail in Fig. 9. In all four selected grid cells (a-d), the posterior uncertainty not only decreases significantly but also becomes very close to a normal distribution, despite the larger and lognormal distributed prior uncertainty. However, what becomes apparent is, that in all of this 4 cases, emissions shift to smaller posterior values relative to the prior, suggesting that negative emission increments favor error reduction and the transition towards normality.

To further investigate this behavior, Fig. 10 compares the ensemble distributions in two representative grid cells: one exhibiting a positive inversion increment (upper panel) and one exhibiting a negative increment (lower panel). For each grid cell, the prior and posterior distributions are shown both in linear space (left panels, in terms of $\mathbf{x}$) and in log space (right panels, in

https://doi.org/10.5194/egusphere-2026-2125
Preprint. Discussion started: 5 June 2026

terms of $\mathbf{z} = \ln(\mathbf{x}/\mathbf{x}_b)$). In addition, Fig. 11 presents maps of the relative uncertainty reduction in (a) linear space and (b) log space, while panel (c) shows the inversion increments together with the locations of the two selected grid cells.

In linear space, the prior distribution is lognormal. For the grid cell with a positive increment, the posterior distribution is shifted toward larger values of $\mathbf{x}$ and remains close to lognormal, even though its mode moves closer to the center of the distribution. The posterior uncertainty even slightly increases compared to the prior, as indicated by the standard deviation values reported in the upper right of each panel. In contrast, for the grid cell with a negative increment, the posterior distribution is shifted toward smaller values and becomes much narrower, approaching a Gaussian shape. This behavior directly translates into a strongly asymmetric (relative) error reduction in linear space (Fig. 11a), with excessively large reductions for negative increments, while positive increments exhibit only weak reductions or, in some cases, even an apparent increase in uncertainty. This asymmetry is not an artifact of the inversion, but arises naturally from the properties of the lognormal prior, whose variance in linear space is intrinsically tied to the absolute value of the emissions. As shown in the Appendix, the observed behavior emerges mathematically when the posterior uncertainty is approximated from the curvature of the cost function. However, this strong asymmetry complicates the interpretation of uncertainty reduction in linear space, as changes in absolute emission magnitude conflate with the actual information content provided by the observations. Negative error reduction, in particular, can be misleading, as it does not necessarily imply that observations degrade the solution, but instead reflect the dependence of the variance on the absolute emission value under a lognormal prior. This motivates an analysis in log space, where uncertainties are much more symmetric (Fig. 10, right). Both prior and posterior emissions are approximately normally distributed and in both grid cells, the posterior uncertainty is reduced relative to the prior (Fig. 10, lower panel). Consequently, the error reduction map in log space (Fig. 11b) exhibits only positive values and is strongly governed by the emission sensitivity, in agreement with the uncertainty approximation derived in the Appendix. Note, however, that also in log space a weaker asymmetry associated with the likelihood remains. This is likely reflected in the relatively small uncertainty reductions observed for the grid cells with large positive increments in southwest Germany.

Finally, Fig. 12 shows the map of the gridded absolute posterior uncertainty derived from the Monte Carlo ensemble. While the posterior distribution is approximately Gaussian in many grid cells, it remains distinctly lognormal in others, rendering the standard deviation an inappropriate measure of uncertainty. We therefore define the posterior uncertainty as half the 16th–84th percentile range of the ensemble, which reduces the influence of the inherent asymmetry of the lognormal distribution.

5 Conclusions

In this study, we investigated the implementation of a lognormal priori probability distribution for atmospheric inversions. We presented the formal implementation in a variational inversion framework, optimizing for three different parameters: mean, median, and mode. We evaluated the performance with synthetic and real data experiments, using a case study of European SF_6 inversions and discussed the estimation of the posterior uncertainties using a Monte Carlo approach. The key points of our study are the following:

https://doi.org/10.5194/egusphere-2026-2125
Preprint. Discussion started: 5 June 2026

- Gridded emission inventories, which are often used as prior information in inversions, frequently exhibit lognormal distributions, as demonstrated for the example of SF_6. In such cases, it is likely that the associated uncertainties are also better represented by a lognormal rather than a normal distribution.

- For a lognormal distribution mean, median, and mode do not fall together making it necessary to choose explicitly which of these parameters to optimize for in the inversion.

- Optimizing for the mode and the mean can yield improved emission estimates when the observational constraints are strong. However, under weak observational constraints, these choices can lead to unstable and strongly biased inversion results caused by a decrease in the cost in the state space due to the extra logarithm term in the cost functions.

- Optimizing for the median consistently improved prior emissions across all tested cases, and thus provides the most robust estimator to optimize for.

- The lognormal based inversion produced a posterior emission pattern that is overall very similar to the one obtained using a normal distribution. However, it prevented non-physical negative emission values and may have also avoided the overestimation of nearby emissions, which might occur in normal-based inversions as a compensatory effect for negative values. Further, the lognormal prior distribution occasionally allowed for stronger positive emission adjustments compared to the Gaussian, likely due to the long tail of the distribution.

- The posterior uncertainties can be estimated using a Monte Carlo approach by creating an ensemble of inversions, each with prior emissions perturbed by lognormally distributed errors. However, we find that the resulting distributions are strongly influenced by the sign of the inversion increment. Negative increments typically lead to narrow, nearly Gaussian posterior distributions, while positive increments are associated with broader and more skewed, lognormal-shaped distributions. To account for this asymmetry, we recommend characterizing posterior uncertainty using interpercentile ranges derived from the ensemble, rather than the standard deviation.

- The error reduction in linear space is highly asymmetric with respect to the sign of the inversion increments, which complicates its interpretation as a measure of the information content provided by the observations. We therefore recommend assessing error reduction in log space, which exhibits much weaker asymmetries, and is therefore better suited to reflect the observational constraints.

Code and data availability. Atmospheric SF_6 mole fractions data used in this study were obtained from the following sources: AGAGE data: https://doi.org/10.15485/1909711 (Prinn et al., 2023); Heathfield Tall Tower data: https://catalogue.ceda.ac.uk/uuid/df502fe4715c4177ab5e4e367a99316b (Arnold et al., 2019); Bilsdale Tall Tower data: https://catalogue.ceda.ac.uk/uuid/d2090552c8fe4c16a2fd7d616adc2d9f (O'Doherty et al., 2019); Ridge Hill data, Zugspitze-Schneefernerhaus data: https://doi.org/10.50849/WDCGG_SF6_ALL_2022 (di Sarra et al., 2022). All used observations and a priori emission datasets are available at https://doi.org/10.25365/phaidra.812. The lognormal optimization algorithms were implemented in the inversion framework, FLEXINVERT+, available from the Git repository: https://git.nilu.no/flexpart/flexinvertplus.git

https://doi.org/10.5194/egusphere-2026-2125
Preprint. Discussion started: 5 June 2026

and from: https://doi.org/10.25365/phaidra.753 (Thompson, 2025). The FLEXPART sensitivity fields used can be downloaded from https://phaidra.univie.ac.at/o:2343194. Daily global SF_6 mole fraction background fields are available at https://doi.org/10.25365/phaidra.489 (Vojta et al., 2024).

Author contributions. RT and MV designed the study with input from IP. RT developed the algorithms and implemented the code into FLEXINVERT+ in collaboration with IP and MV, MV carried out the evaluation and investigated the a posteriori uncertainties with input from RT. MV and RT wrote the text with contributions from IP.

Competing interests. Ignacio Pisso is a member of the editorial board of Geoscientific Model Development.

Acknowledgements. We sincerely thank the AGAGE team for their contribution of measurement data, including Martin K. Vollmer and Stefan Reimann (Empa, Swiss Federal Laboratories for Materials Science and Technology); Simon O'Doherty, Kieran Stanley, Joseph Pitt, Dickon Young (University of Bristol); Chris Rennick (National Physical Laboratory); and Chris Rene Lunder and Ove Hermanson (NILU).

The operation of AGAGE stations at Mace Head, has been supported by NASA (USA) grants to MIT (grant number NAG5-12669) and SIO (grant number NNX07AE87G). The UK measurements were funded by the UK Government Department for Energy Security and Net Zero (DESNZ) under contracts TRN1028/06/2015, TRN1537/06/2018 and TRN5488/11/2021 to the University of Bristol and through the National Measurement System, funded by the UK Department for Science, Innovation and Technology, at the National Physical Laboratory.

For Jungfraujoch, funding from the Swiss Federal Office for the Environment (FOEN) is acknowledged for the HALCLIM/CLIMGAS-CH project, as well as financial support from ICOS Switzerland (ICOS-CH) Phase 3 (Swiss National Science Foundation, grant 20F120_198227). Observations are further supported by the International Foundation High Altitude Research Stations Jungfraujoch and Gornergrat (HFSJG). The halocarbon measurements at Zeppelin Observatory are supported by the Norwegian Environment Agency.

We thank Cedric Couret (German Environment Agency). Measurements at Zugspitze-Schneefernerhaus, a Global Atmosphere Watch (GAW) station, are supported by the German Environment Agency. We also sincerely thank Pallav Purohit (IIASA, International Institute for Applied Systems Analysis) for providing GAINS SF_6 emissions data. Finally, we thank Steven Fletcher for his valuable input!

The computational results were partly achieved using the Vienna Scientific Cluster (VSC), project number 71878, for a demonstration of a Lagrangian re-analysis. We also acknowledge the use of ECMWF's computing and archive facilities, provided through a special project (spatvojt).

M. Vojta was supported in part by the Edu4ClimAte program, funded by the European Commission (Horizon Europe) under grant agreement number 101071247. R. Thompson received financial support from the ReGAME project funded by the Research Council of Norway (grant no.325610).

https://doi.org/10.5194/egusphere-2026-2125
Preprint. Discussion started: 5 June 2026

Mean

$$J_{mean}(\boldsymbol{x}) = -\frac{1}{2}\left(\ln(\boldsymbol{x}/\boldsymbol{x}_b)\right)^{\mathrm{T}}\mathbf{1} + \frac{1}{2}\left(\ln(\boldsymbol{x}) - \ln(\boldsymbol{x}_b)\right)^{\mathrm{T}}\boldsymbol{\Sigma}^{-1}\left(\ln(\boldsymbol{x}) - \ln(\boldsymbol{x}_b)\right) + \frac{1}{2}(H(\boldsymbol{x}) - \boldsymbol{y})^{\mathrm{T}}\mathbf{R}^{-1}(H(\boldsymbol{x}) - \boldsymbol{y})$$

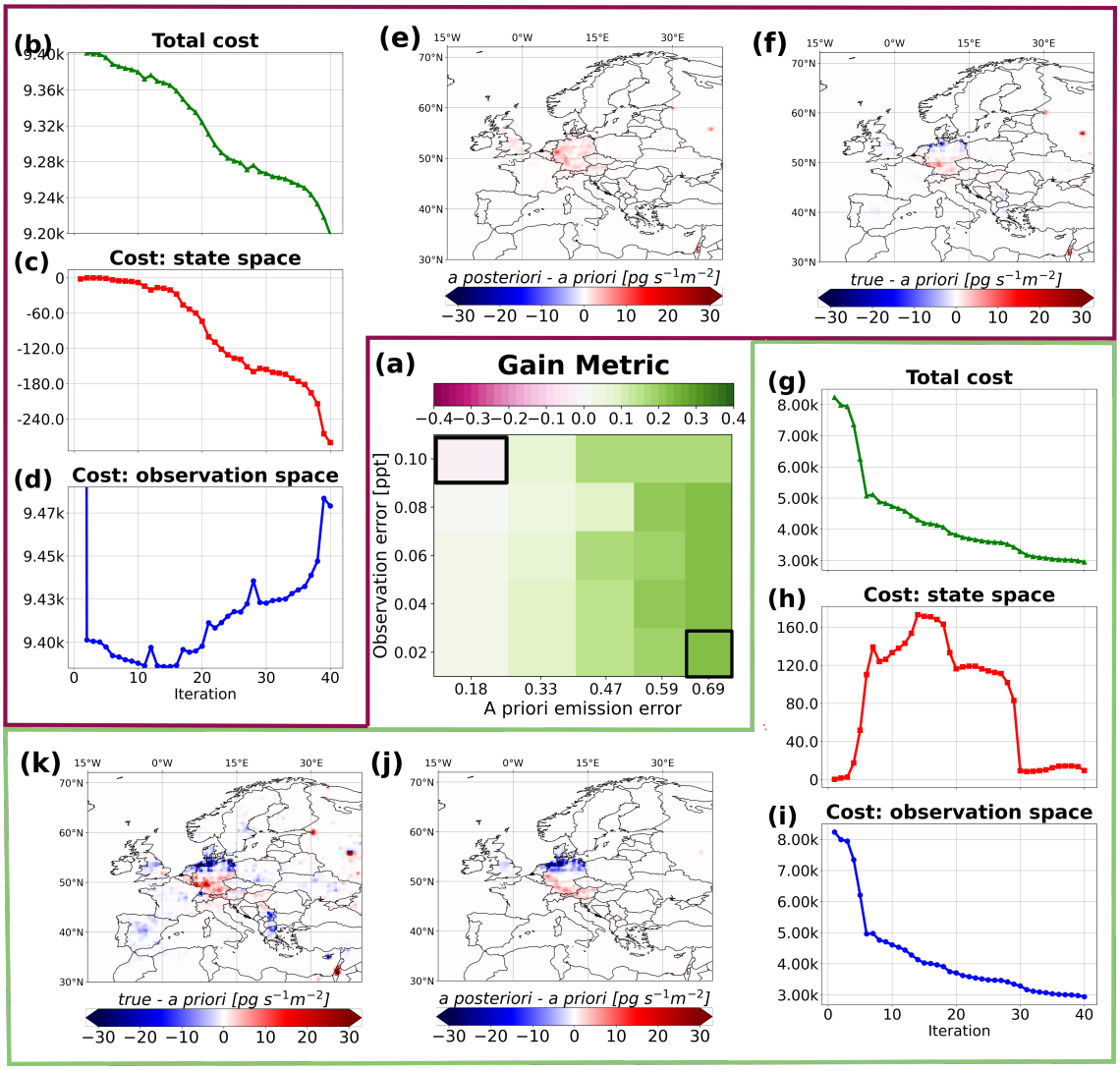

Figure 5. (a) Gain metric for 25 inversions, optimizing for the mean and using different uncertainty settings. Panels (b–d) show the evolution of the total cost (b), state space cost (c), and observation space cost (d) for the case with the weakest observational constraint, while panels (e–f) show the corresponding inversion increments (e) and negative perturbations (f). Panels (g–i) show the evolution of the total (g), state space (h), and observation space (i) cost for the case with the strongest observational constraint, and panels (j–k) show the respective inversion increments (j) and negative perturbations (k).

https://doi.org/10.5194/egusphere-2026-2125
Preprint. Discussion started: 5 June 2026

Median

$$J_{\text{med}}(\boldsymbol{x}) = \frac{1}{2}\left(\ln(\boldsymbol{x}) - \ln(\boldsymbol{x}_b)\right)^{\mathrm{T}}\boldsymbol{\Sigma}^{-1}\left(\ln(\boldsymbol{x}) - \ln(\boldsymbol{x}_b)\right) + \frac{1}{2}(H(\boldsymbol{x}) - \boldsymbol{y})^{\mathrm{T}}\mathbf{R}^{-1}(H(\boldsymbol{x}) - \boldsymbol{y})$$

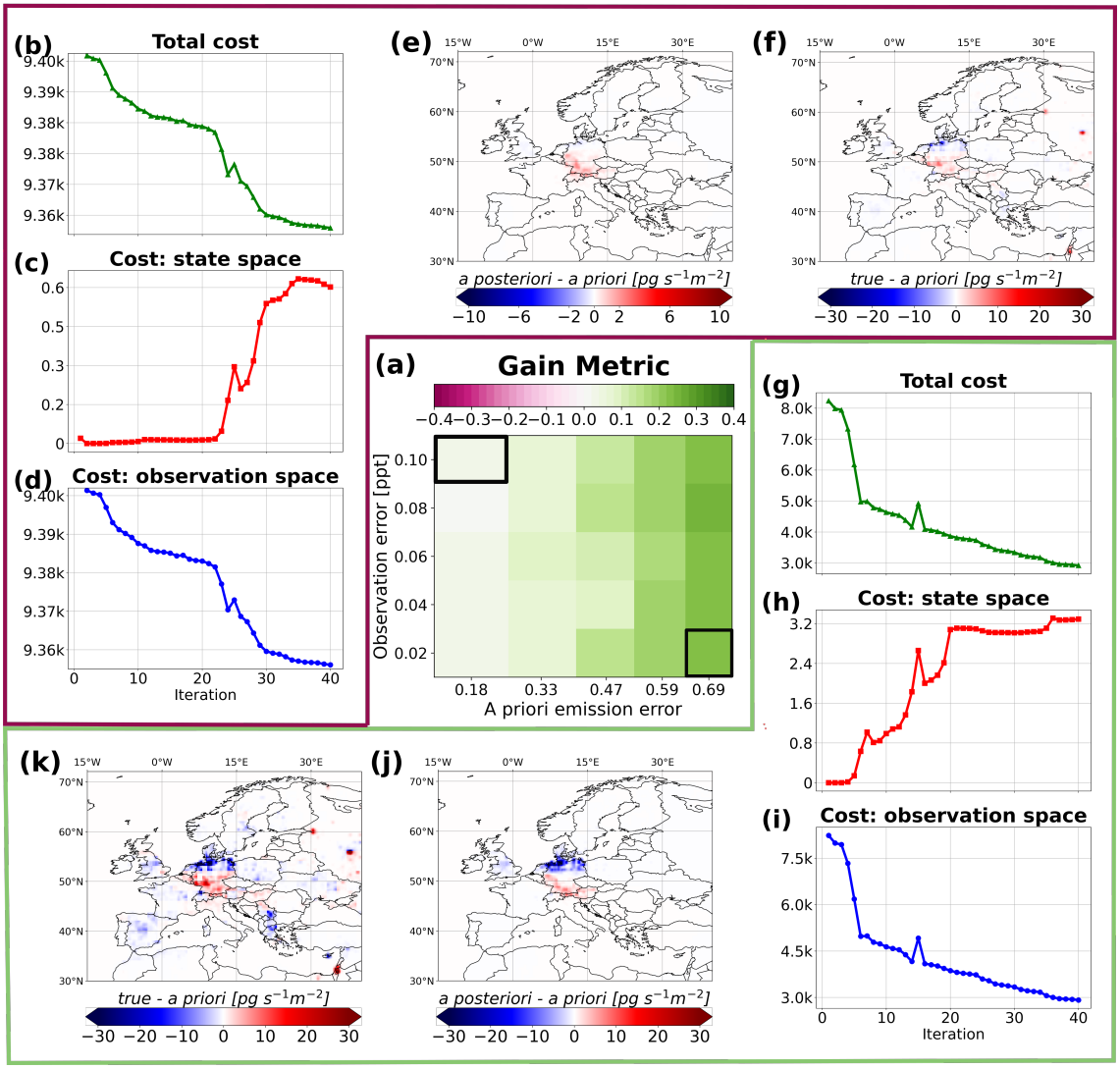

Figure 6. (a) Gain metric for 25 inversions, optimizing for the median and using different uncertainty settings. Panels (b–d) show the evolution of the total cost (b), state space cost (c), and observation space cost (d) for the case with the weakest observational constraint, while panels (e–f) show the corresponding inversion increments (e) and negative perturbations (f). Panels (g–i) show the evolution of the total (g), state space (h), and observation space (i) cost for the case with the strongest observational constraint, and panels (j–k) show the respective inversion increments (j) and negative perturbations (k).

https://doi.org/10.5194/egusphere-2026-2125
Preprint. Discussion started: 5 June 2026

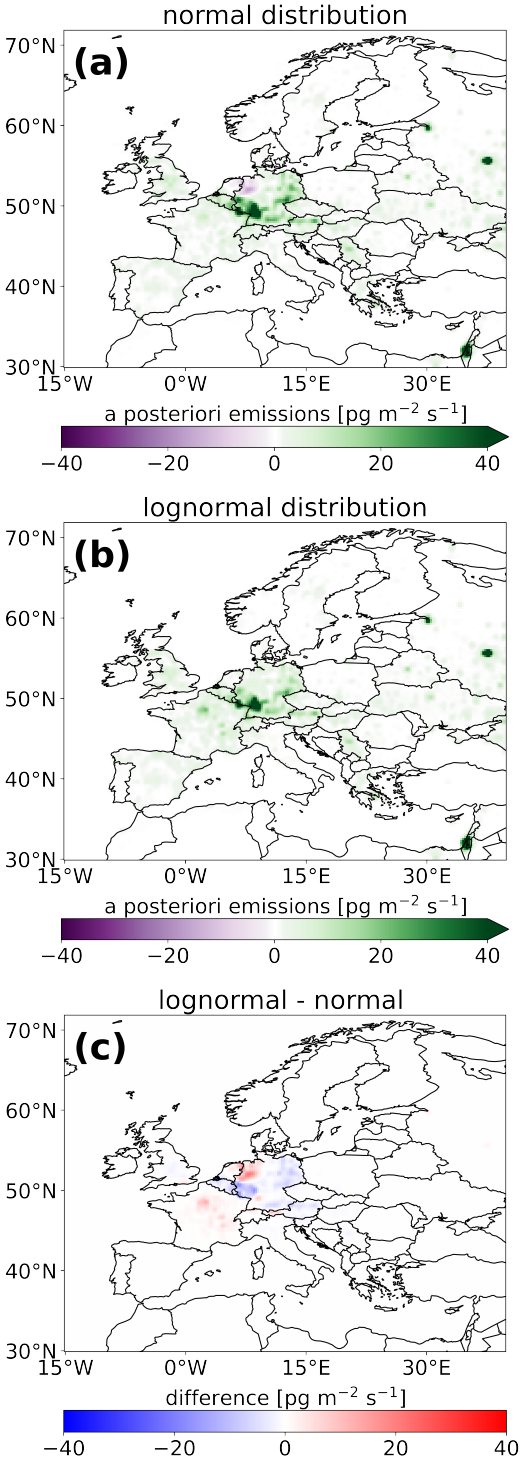

Figure 7. A posteriori emissions resulting from inversions with (a) a normal and (b) a lognormal prior probability distribution. (c) Difference between the two cases.

https://doi.org/10.5194/egusphere-2026-2125
Preprint. Discussion started: 5 June 2026

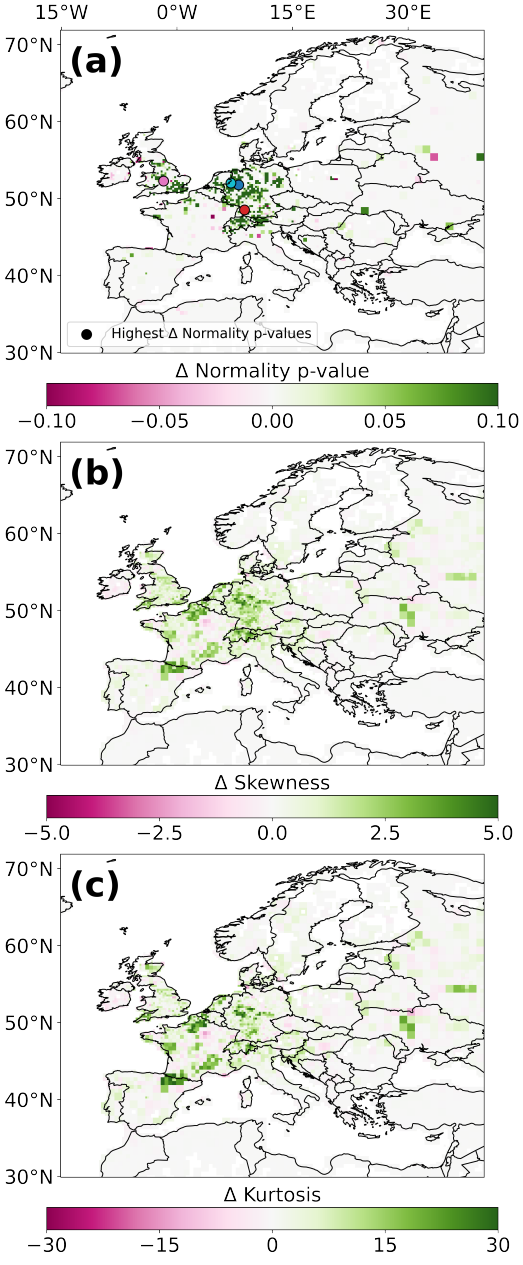

Figure 8. Changes from prior to posterior uncertainty illustrated by differences in (a) p-value (posterior - prior), (b) skewness (prior - posterior), and (c) kurtosis (prior - posterior) of the uncertainty distributions.

https://doi.org/10.5194/egusphere-2026-2125
Preprint. Discussion started: 5 June 2026

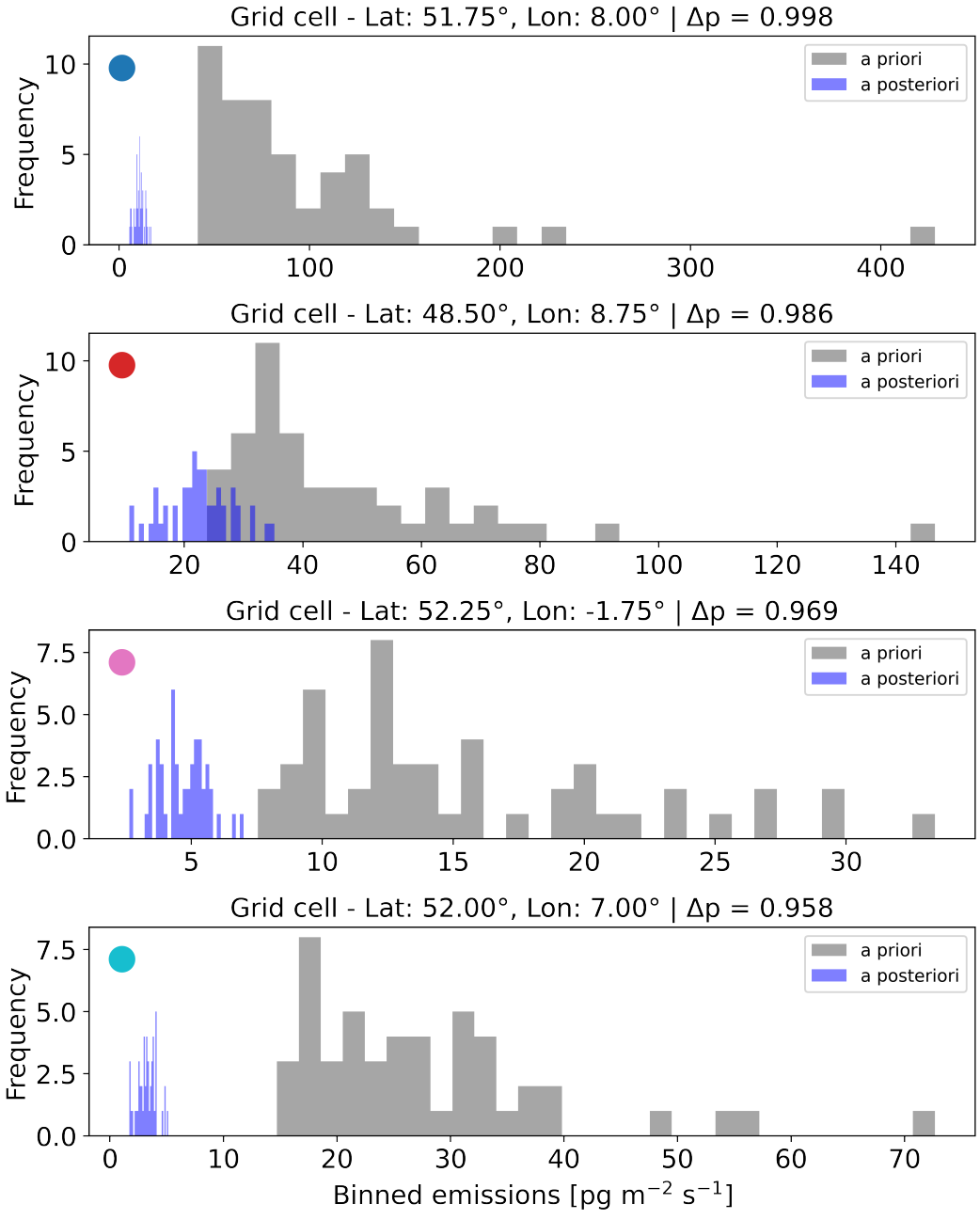

Figure 9. The prior and posterior uncertainty distribution shown for the four grid cells with the largest increases in p-values.

https://doi.org/10.5194/egusphere-2026-2125
Preprint. Discussion started: 5 June 2026

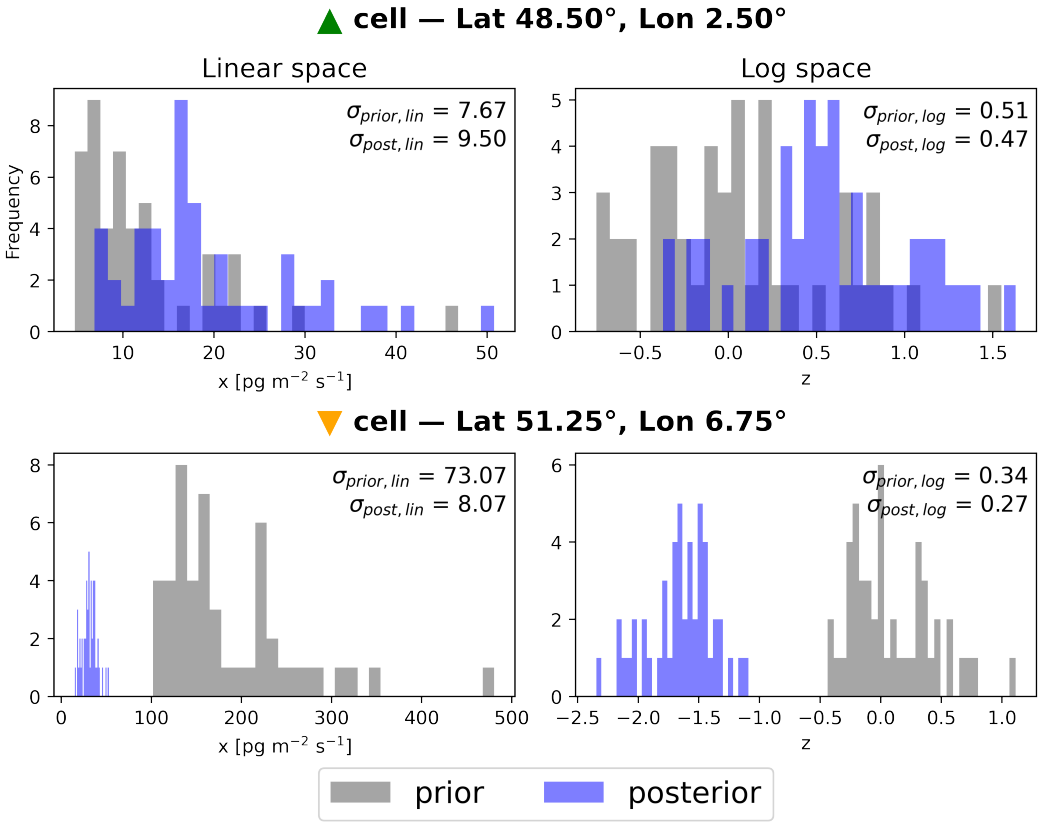

Figure 10. Prior and posterior distribution for a grid cell exhibiting a positive emission increment (upper panel) and for a grid cell with negative increment (lower panel). The distributions are show in the linear space (left) and in the log space (right). The values in the upper-right corner of each panel show the standard deviation (linear space: $\mathrm{pg\,m^{-2}\,s^{-1}}$; log space: dimensionless).

https://doi.org/10.5194/egusphere-2026-2125
Preprint. Discussion started: 5 June 2026

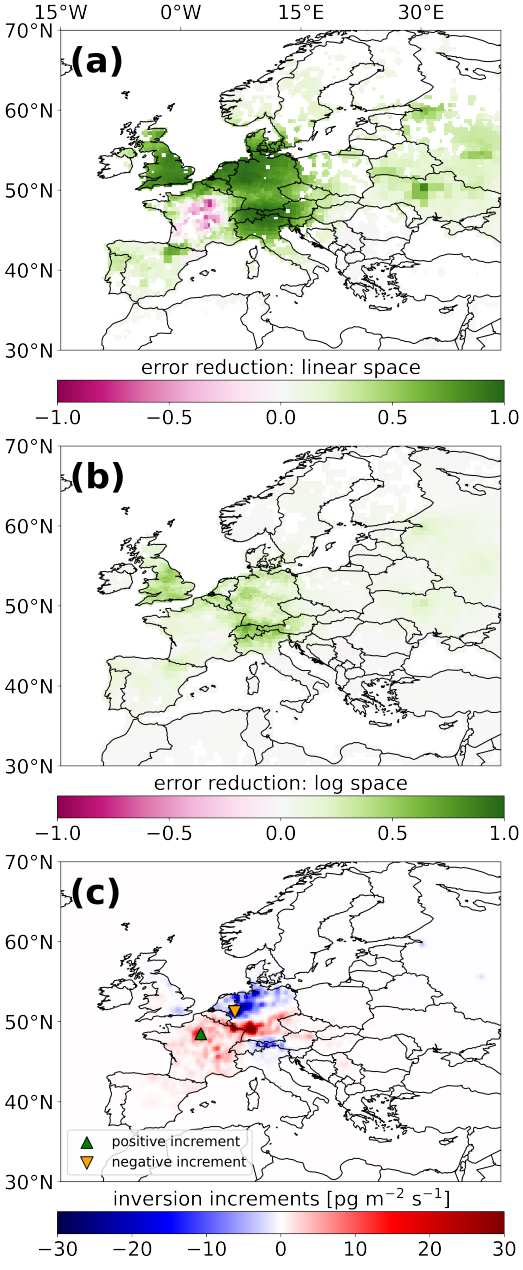

Figure 11. Relative error reduction in (a) linear space and (b) log space. (c) shows the inversion increments together with the location of the further investigated grid cells

https://doi.org/10.5194/egusphere-2026-2125
Preprint. Discussion started: 5 June 2026

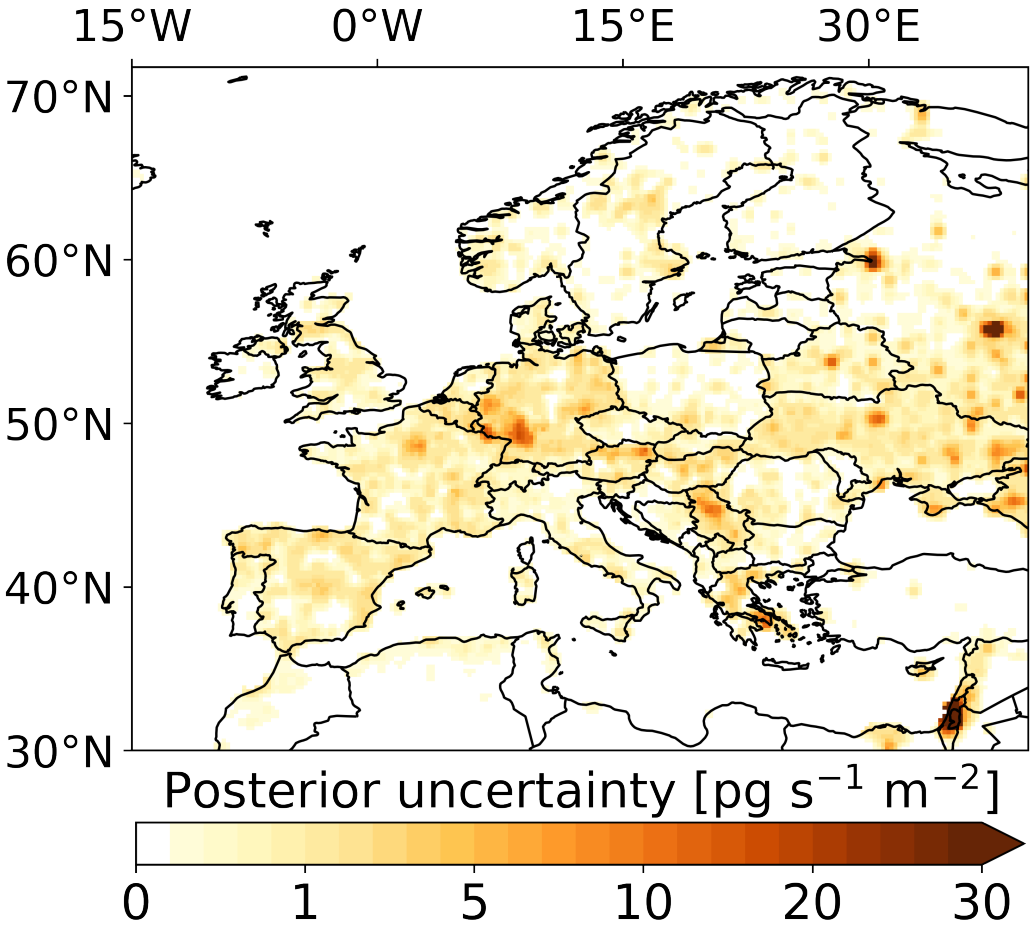

Figure 12. Ensemble-based a posteriori uncertainty, defined as half of the 16th–84th percentile range

https://doi.org/10.5194/egusphere-2026-2125
Preprint. Discussion started: 5 June 2026

Appendix A: The posterior uncertainty

In this Appendix, we investigate the asymmetries discussed in Sect. 4.2.2 in the posterior uncertainties of our Monte Carlo ensemble. Our posterior distribution arises from the combination of a Gaussian likelihood and a lognormal prior. We characterize its uncertainty by using a Laplace approximation (e.g. MacKay, 1992) in one dimension, approximating the posterior variance by the inverse of the curvature of the cost function evaluated at the MAP estimate.

Therefore we write the posterior probability in terms of the cost function $J(x)$:

$$P(x \mid y) \propto \exp(-J(x)) \tag{A1}$$

and approximate $J(x)$ near the minimum by a quadratic expansion:

$$J(x) \approx J(x_{\mathrm{MAP}}) + \frac{1}{2} J''(x_{\mathrm{MAP}}) (x - x_{\mathrm{MAP}})^2, \tag{A2}$$

so that Eq.A1 becomes:

$$P(x \mid y) \propto \exp\left[-\frac{1}{2} J''(x_{\mathrm{MAP}}) (x - x_{\mathrm{MAP}})^2\right]. \tag{A3}$$

By comparing with a standard Gaussian $\mathcal{N}(x_{\mathrm{MAP}}, \sigma^2_{\mathrm{post}})$, we obtain :

$$\sigma^2_{\mathrm{post}} \approx [J''(x_{\mathrm{MAP}})]^{-1}. \tag{A4}$$

If the optimization results in a posterior that is close to Gaussian, this approximation will be accurate. If the posterior remains closer to a lognormal distribution, the associated uncertainty may be underestimated, as it does not fully capture the skewness of the distribution. Similarly, when optimizing for the mean or median, instead of the mode, the uncertainty formulation is not exact for skewed posteriors. However, these limitations do not affect the qualitative discussions of our analysis.

A1 Linear space

To be consistent with the approximation around x_{MAP} let's consider now the cost function for the mode (see Eq. 14) in one dimension:

$$J(x) = \ln\left(\frac{x}{x_b}\right) + \frac{1}{2\sigma^2_{b,log}} \left[\ln\left(\frac{x}{x_b}\right)\right]^2 + \frac{1}{2\sigma^2_o} (y - hx)^2. \tag{A5}$$

The second derivative in the linear space is:

https://doi.org/10.5194/egusphere-2026-2125
Preprint. Discussion started: 5 June 2026

$$J''(x) = \frac{1}{\sigma_{b,log}^2 x^2}\left(1 - \ln\left(\frac{x}{x_b}\right) - \sigma_{b,log}^2\right) + \frac{1}{\sigma_o^2}h^2 \tag{A6}$$

and the expression for the posterior variance in the linear space reads[3]:

$$\sigma^2_{\text{post, lin}} \approx \left(\frac{h^2}{\sigma_o^2} + \frac{1 - \ln\left(\frac{x_{\text{MAP}}}{x_b}\right) - \sigma_{b,log}^2}{\sigma_{b,log}^2 x_{\text{MAP}}^2}\right)^{-1}. \tag{A7}$$

Equation A7 reflects the asymmetry arising from the lognormal prior and how it depends on the sign of the inversion increments. Let's consider a grid cell with a small posterior estimate, which is much smaller than the prior (as shown in Fig. 9). In this case, the curvature grows with increasingly negative increment, which reduces the posterior uncertainty. Conversely, if the inversion increment is positive, the curvature decreases with growing increment leading to a larger posterior uncertainty. This asymmetry is particularly pronounced when emissions are poorly constrained, that is, when the prior term dominates the optimization. Notice, that the logarithm $\ln\left(\frac{x_{\text{MAP}}}{x_b}\right)$ is steeper for values below the prior mode ($x < x_b$) than above ($x > x_b$), so negative increments have likely a stronger effect on the curvature than positive increments of the same magnitude.

As a result of this asymmetry, also the error reduction in the linear space is highly asymmetric: larger for negative increments and smaller for positive increments, and in case of poor observational constraint and large positive increments, it might even become negative. Note, that in extreme cases, in principal, the entire expression for the posterior variance may become negative, which would make the posterior uncertainty formally imaginary, which signals that our approximation (Eq. A2) is breaking down.

A2 Log space

Let's now write the cost function (Eq.A5) in terms of $z = ln(x/x_b)$:

$$J(z) = z + \frac{1}{2\sigma_{b,log}^2}z^2 + \frac{1}{2\sigma_o^2}(y - hx_b e^z)^2. \tag{A8}$$

The second derivative in respect to z is:

$$J''(z) = \frac{1}{\sigma_{b,log}^2} + \frac{hx_b e^z\,(2hx_b e^z - y)}{\sigma_o^2} \tag{A9}$$

and the posterior uncertainty in the log space becomes:

$$\sigma^2_{\text{post},log} \approx \left[\frac{1}{\sigma_{b,log}^2} + \frac{h\,x_b\,e^{z_{\text{MAP}}}\left(2\,h\,x_b\,e^{z_{\text{MAP}}} - y\right)}{\sigma_o^2}\right]^{-1}. \tag{A10}$$

[3]Note that although we define the posterior variance in linear space, the prior variance is still expressed in log space.

https://doi.org/10.5194/egusphere-2026-2125
Preprint. Discussion started: 5 June 2026

While the linear-space variance is highly asymmetric due to the prior term, the log-space prior term becomes constant. However Eq. A10 shows some asymmetry in the likelihood. To better discuss this, let's substitute $x_{MAP} = x_b\, e^{z_{\mathrm{MAP}}}$:

$$\sigma^2_{\mathrm{post},log} \approx \left[\frac{1}{\sigma^2_{b,log}} + \frac{h\,x_{MAP}\left(2\,h\,x_{MAP} - y\right)}{\sigma^2_o}\right]^{-1}. \tag{A11}$$

In case of a good model-measurement agreement ($h\,x_{MAP} \approx y$), the curvature of the likelihood approaches $(hx)^2\,\sigma_o^{-2}$, and the posterior uncertainty in log space is primarily controlled by the observational signal. However, for large residuals between $h\,x_{\mathrm{MAP}}$ and y, the curvature becomes explicitly dependent on the sign and magnitude of the mismatch. This effect could be relevant for strong point sources detected by the inversion, where observations indicate much larger emissions than suggested by the prior and large model-observation mismatches may persist even after the inversion, leading to a reduced curvature and comparatively large posterior uncertainties in the affected grid cells.

Let's now define the uncertainty reduction in the log-space as

$$r_{\log} = 1 - \frac{\sigma_{\mathrm{post,log}}}{\sigma_{b,\log}}. \tag{A12}$$

Using Eq. A11, this can be written as

$$r_{\log} \approx 1 - \left[1 + \frac{\sigma^2_{b,\log}}{\sigma^2_o} h\,x_{MAP}\left(2\,h\,x_{MAP} - y\right)\right]^{-\frac{1}{2}}. \tag{A13}$$

Similar to the posterior uncertainty, the uncertainty reduction is primarily controlled by the observational signal, however, asymmetries can arise through large model-observation mismatches.

https://doi.org/10.5194/egusphere-2026-2125
Preprint. Discussion started: 5 June 2026

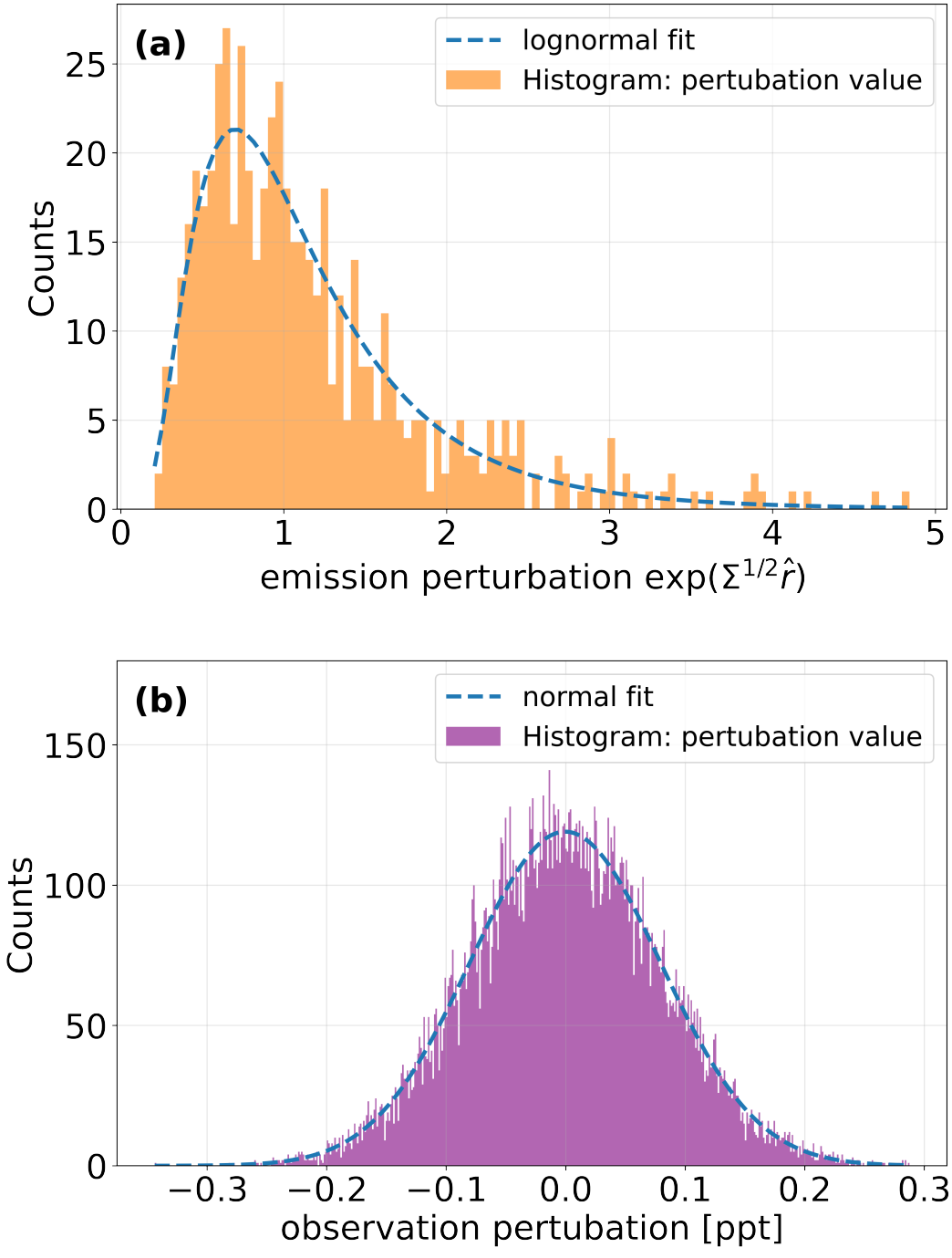

Figure A1. (a) Histogram of the emission perturbation factor, $\exp(\boldsymbol{\Sigma}^{1/2}\hat{\boldsymbol{r}})$, based on a prior error covariance matrix $\boldsymbol{\Sigma}$, with an uncertainty of 0.59 and (b) histogram of the observation perturbation, $\mathbf{R}^{1/2}\hat{\boldsymbol{r}}$, corresponding to a measurement error of 0.08 ppt.

https://doi.org/10.5194/egusphere-2026-2125
Preprint. Discussion started: 5 June 2026

References

Arnold, T., Rennick, C., O'Doherty, S., Say, D., Young, D., Stavert, A., and Wenger, A.: Deriving Emissions related to Climate Change Network: CO2, CH4, N2O, SF6 and CO measurements from Heathfield Tall Tower, East Sussex. Centre for Environmental Data Analysis, https://catalogue.ceda.ac.uk/uuid/df502fe4715c4177ab5e4e367a99316b, last accessed: 2024-02-1, 2019.

Brioude, J., Kim, S.-W., Angevine, W. M., Frost, G., Lee, S.-H., McKeen, S., Trainer, M., Fehsenfeld, F. C., Holloway, J., Ryerson, T., et al.: Top-down estimate of anthropogenic emission inventories and their interannual variability in Houston using a mesoscale inverse modeling technique, Journal of Geophysical Research: Atmospheres, 116, https://doi.org/10.1029/2011JD016215, 2011.

Chen, Z., Jacob, D. J., Gautam, R., Omara, M., Stavins, R. N., Stowe, R. C., Nesser, H., Sulprizio, M. P., Lorente, A., Varon, D. J., et al.: Satellite quantification of methane emissions and oil–gas methane intensities from individual countries in the Middle East and North Africa: implications for climate action, Atmospheric Chemistry and Physics, 23, 5945–5967, https://doi.org/10.5194/acp-23-5945-2023, 2023.

Cohn, S. E.: An Introduction to Estimation Theory, Journal of the Meteorological Society of Japan, 75, 257–288, https://doi.org/10.2151/jmsj1965.75.1B_257, 1997.

Crippa, M., D., G., Pagani, F., Banja, M., Muntean, M., E., S., Becker, W., Monforti-Ferrario, F., Quadrelli, R., Risquez Martin, A., Taghavi-Moharamli, P., Köykkä, J., Grassi, G., Rossi, S., Brandao De Melo, J., Oom, D., Branco, A., San-Miguel, J., and Vignati, E.: GHG emissions of all world countries, Publications Office of the European Union, Luxembourg, 2023, https://doi.org/10.2760/953322, 2023.

di Sarra, A., Hall, B. D., Dylag, C., Couret, C., Lunder, C., Sweeney, C., Sferlazzo, D., Say, D., Mondeel, D. J., Young, D., Dlugokencky, E., Cuevas, E., Meinhardt, F., Technos, G. E., Dutton, G. S., Lee, H., Nance, J. D., Arduini, J., Pitt, J., Tsuboi, K., Stanley, K., Gatti, L. V., Steinbacher, M., Vollmer, M., Krummel, P., Rivas, P., Weiss, R. F., Wang, R., Chiavarini, S., Piacentino, S., O'Doherty, S., Reimann, S., A. Montzka, S., Saito, T., and Lan, X.: All SF6 data contributed to WDCGG by GAW stations and mobiles by 2022-09-05, https://doi.org/10.50849/WDCGG_SF6_ALL_2022, 2022.

D'Agostino, R. and Pearson, E. S.: Tests for departure from normality, Biometrika, 60, 613–622, https://doi.org/10.1093/biomet/60.3.613, 1973.

EDGAR: (Emissions Database for Global Atmospheric Research) Community GHG Database version 8.0, European Commission, Joint Research Centre (JRC), the International Energy Agency (IEA), Datasets, https://edgar.jrc.ec.europa.eu/dataset_ghg80, last accessed: 2024-01-27, 2023.

Evangeliou, N., Thompson, R. L., Eckhardt, S., and Stohl, A.: Top-down estimates of black carbon emissions at high latitudes using an atmospheric transport model and a Bayesian inversion framework, Atmospheric Chemistry and Physics, 18, 15 307–15 327, https://doi.org/10.5194/acp-18-15307-2018, 2018.

Fletcher, S. and Zupanski, M.: A data assimilation method for log-normally distributed observational errors, Quarterly Journal of the Royal Meteorological Society: A journal of the atmospheric sciences, applied meteorology and physical oceanography, 132, 2505–2519, https://doi.org/10.1256/qj.05.222, 2006.

Fletcher, S. J., Kliewer, A. J., and Jones, A. S.: Quantification of optimal choices of parameters in lognormal Variational data assimilation and their chaotic behavior, Mathematical Geosciences, 51, 187–207, https://doi.org/10.1007/s11004-018-9765-7, 2019.

Ganesan, A. L., Rigby, M., Zammit-Mangion, A., Manning, A. J., Prinn, R. G., Fraser, P. J., Harth, C. M., Kim, K.-R., Krummel, P. B., Li, S., Mühle, J., O'Doherty, S. J., Park, S., Salameh, P. K., Steele, L. P., and Weiss, R. F.: Characterization of uncertainties in atmospheric trace

https://doi.org/10.5194/egusphere-2026-2125
Preprint. Discussion started: 5 June 2026

gas inversions using hierarchical Bayesian methods, Atmospheric Chemistry and Physics, 14, 3855–3864, https://doi.org/10.5194/acp-14-3855-2014, 2014.

Gilbert, J. C. and Lemaréchal, C.: The module M1QN3, INRIA Rep., version, 3, 21, https://who.paris.inria.fr/Jean-Charles.Gilbert/preprint/u01-m1qn3.pdf, last accessed: 2025-02-29, 2006.

Henne, S., Brunner, D., Oney, B., Leuenberger, M., Eugster, W., Bamberger, I., Meinhardt, F., Steinbacher, M., and Emmenegger, L.: Validation of the Swiss methane emission inventory by atmospheric observations and inverse modelling, Atmospheric Chemistry and Physics, 16, 3683–3710, https://doi.org/10.5194/acp-16-3683-2016, 2016.

Legras, B., Joseph, B., and Lefèvre, F.: Vertical diffusivity in the lower stratosphere from Lagrangian back-trajectory reconstructions of ozone profiles, Journal of Geophysical Research: Atmospheres, 108, 4562, https://doi.org/10.1029/2002JD003045, 2003.

Legras, B., Pisso, I., Berthet, G., and Lefèvre, F.: Variability of the Lagrangian turbulent diffusion in the lower stratosphere, Atmospheric Chemistry and Physics, 5, 1605–1622, https://doi.org/10.5194/acp-5-1605-2005, 2005.

Limpert, E., Stahel, W. A., and Abbt, M.: Log-normal distributions across the sciences: keys and clues: on the charms of statistics, and how mechanical models resembling gambling machines offer a link to a handy way to characterize log-normal distributions, which can provide deeper insight into variability and probability—normal or log-normal: that is the question, BioScience, 51, 341–352, https://doi.org/10.1641/0006-3568(2001)051[0341:LNDATS]2.0.CO;2, 2001.

Lorenc, A. C.: Analysis methods for numerical weather prediction, Quarterly Journal of the Royal Meteorological Society, 112, 1177–1194, https://doi.org/10.1002/qj.49711247414, 1986.

MacKay, D. J. C.: Bayesian interpolation, Neural Computation, 4, 415–447, https://doi.org/10.1162/neco.1992.4.3.415, 1992.

Manning, A., Redington, A., O'Doherty, S., Say, D., Young, D., Arnold, T., Rennick, C., Rigby, M., Wisher, A., and Simmonds, P.: Long-Term Atmospheric Measurement and Interpretation of Radiatively Active Trace Gases–Detailed Report (September 2019 to August 2020), Tech. rep., Department for Business, Energy & Industrial Strategy, https://assets.publishing.service.gov.uk/media/62d7b9bee90e071e7e59c97e/verification-uk-greenhouse-gas-emissions-using-atmospheric-observations-annual-report-2021.pdf, (last access 10 November 2023), 2022.

Manning, A. J., O'Doherty, S., Jones, A. R., Simmonds, P. G., and Derwent, R. G.: Estimating UK methane and nitrous oxide emissions from 1990 to 2007 using an inversion modeling approach, Journal of Geophysical Research: Atmospheres, 116, https://doi.org/10.1029/2010JD014763, _eprint: https://agupubs.onlinelibrary.wiley.com/doi/pdf/10.1029/2010JD014763, 2011.

O'Doherty, S., Say, D., Stanley, K., Young, D., Pitt, J., and Wenger, A.: Deriving Emissions related to Climate Change Network: CO2, CH4, N2O, SF6 and CO measurements from Bilsdale Tall Tower, North York Moors National Park. Centre for Environmental Data Analysis, https://catalogue.ceda.ac.uk/uuid/d2090552c8fe4c16a2fd7d616adc2d9f, last accessed: 2024-02-1, 2019.

Peng, S., Lin, X., Thompson, R. L., Xi, Y., Liu, G., Hauglustaine, D., Lan, X., Poulter, B., Ramonet, M., Saunois, M., et al.: Wetland emission and atmospheric sink changes explain methane growth in 2020, Nature, 612, 477–482, https://doi.org/10.1038/s41586-022-05447-w, 2022.

Pisso, I., Sollum, E., Grythe, H., Kristiansen, N. I., Cassiani, M., Eckhardt, S., Arnold, D., Morton, D., Thompson, R. L., Groot Zwaaftink, C. D., Evangeliou, N., Sodemann, H., Haimberger, L., Henne, S., Brunner, D., Burkhart, J. F., Fouilloux, A., Brioude, J., Philipp, A., Seibert, P., and Stohl, A.: The Lagrangian particle dispersion model FLEXPART version 10.4, Geoscientific Model Development, 12, 4955–4997, https://doi.org/10.5194/gmd-12-4955-2019, 2019.

https://doi.org/10.5194/egusphere-2026-2125
Preprint. Discussion started: 5 June 2026

Prinn, R., Cunnold, D., Rasmussen, R., Simmonds, P., Alyea, F., Crawford, A., Fraser, P., and Rosen, R.: Atmospheric emissions and trends of nitrous oxide deduced from 10 years of ALE–GAGE data, Journal of Geophysical Research: Atmospheres, 95, 18 369–18 385, https://doi.org/10.1029/JD095iD11p18369, 1990.

Prinn, R., Weiss, R., Arduini, J., Arnold, T., Fraser, P., Ganesan, A., Gasore, J., Harth, C., Hermansen, O., Kim, J., Krummel, P., Loh, Z., Lunder, C., Maione, M., Manning, A., Miller, B., Mitrevski, B., Mühle, J., O'Doherty, S., Park, S., Reimann, S., Rigby, M., Saito, T., Salameh, P., Schmidt, R., Simmonds, P., Steel, P., Vollmer, M. K., Wang, H. R., Yao, B., Young, D., and Zhou, L.: The dataset of in-situ measurements of chemically and radiatively important atmospheric gases from the AGAGE and affiliated stations (2022R2), https://doi.org/10.15485/1909711, version 2022R2, 2023.

Purohit, P. and Höglund-Isaksson, L.: Global emissions of fluorinated greenhouse gases 2005–2050 with abatement potentials and costs, Atmospheric Chemistry and Physics, 17, 2795–2816, https://doi.org/10.5194/acp-17-2795-2017, 2017.

Rayner, P., Enting, I., Francey, R., and Langenfelds, R.: Reconstructing the recent carbon cycle from atmospheric CO2, δ13C and O2/N2 observations, Tellus B: Chemical and Physical Meteorology, 51, 213–232, https://doi.org/10.3402/tellusb.v51i2.16273, 1999.

Rödenbeck, C., Zaehle, S., Keeling, R., and Heimann, M.: How does the terrestrial carbon exchange respond to inter-annual climatic variations? A quantification based on atmospheric CO 2 data, Biogeosciences, 15, 2481–2498, https://doi.org/10.5194/bg-15-2481-2018, 2018.

Rodgers, C. D.: Inverse methods for atmospheric sounding: theory and practice, vol. 2, World scientific, 2000.

Tans, P. P., Conway, T. J., and Nakazawa, T.: Latitudinal distribution of the sources and sinks of atmospheric carbon dioxide derived from surface observations and an atmospheric transport model, Journal of Geophysical Research: Atmospheres, 94, 5151–5172, https://doi.org/10.1029/JD094iD04p05151, 1989.

Tarantola, A.: Inverse Problem Theory and Methods for Model Parameter Estimation, pp. 1–67, Society for Industrial and Applied Mathematics, ISBN 978-0-89871-572-9 978-0-89871-792-1, https://doi.org/10.1137/1.9780898717921, 2005.

Thompson, R. L.: FLEXINVERT+: including lognormal optimization algorithms, https://doi.org/10.25365/phaidra.753, [data set], 2025.

Thompson, R. L. and Stohl, A.: FLEXINVERT: an atmospheric Bayesian inversion framework for determining surface fluxes of trace species using an optimized grid, Geoscientific Model Development, 7, 2223–2242, https://doi.org/10.5194/gmd-7-2223-2014, 2014.

Thompson, R. L., Chevallier, F., Crotwell, A. M., Dutton, G., Langenfelds, R. L., Prinn, R. G., Weiss, R. F., Tohjima, Y., Nakazawa, T., Krummel, P. B., et al.: Nitrous oxide emissions 1999 to 2009 from a global atmospheric inversion, Atmospheric Chemistry and Physics, 14, 1801–1817, https://doi.org/10.5194/acp-14-1801-2014, 2014.

Virtanen, P., Gommers, R., Oliphant, T. E., Haberland, M., Reddy, T., Cournapeau, D., Burovski, E., Peterson, P., Weckesser, W., Bright, J., van der Walt, S. J., Brett, M., Wilson, J., Millman, K. J., Mayorov, N., Nelson, A. R. J., Jones, E., Kern, R., Larson, E., Carey, C. J., Polat, İ., Feng, Y., Moore, E. W., VanderPlas, J., Laxalde, D., Perktold, J., Cimrman, R., Henriksen, I., Quintero, E. A., Harris, C. R., Archibald, A. M., Ribeiro, A. H., Pedregosa, F., van Mulbregt, P., and Contributors, S. .: SciPy 1.0: Fundamental Algorithms for Scientific Computing in Python, Nature Methods, 17, 261–272, https://doi.org/10.1038/s41592-019-0686-2, 2020.

Vojta, M., Plach, A., Thompson, R. L., and Stohl, A.: A comprehensive evaluation of the use of Lagrangian particle dispersion models for inverse modeling of greenhouse gas emissions, Geoscientific Model Development, 15, 8295–8323, https://doi.org/10.5194/gmd-15-8295-2022, 2022.

Vojta, M., Plach, A., Annadate, S., Park, S., Lee, G., Purohit, P., Lindl, F., Lan, X., Mühle, J., Thompson, R. L., et al.: A global re-analysis of regionally resolved emissions and atmospheric mole fractions of SF6 for the period 2005–2021, Atmospheric Chemistry and Physics, 24, 12 465–12 493, https://doi.org/10.5194/acp-24-12465-2024, 2024.

https://doi.org/10.5194/egusphere-2026-2125
Preprint. Discussion started: 5 June 2026

Vojta, M., Plach, A., Thompson, R. L., Purohit, P., Stanley, K., O'Doherty, S., Young, D., Pitt, J., Arduini, J., Lan, X., et al.: Quantifying European SF6 emissions from 2005 to 2021 using a large inversion ensemble, Atmospheric Chemistry and Physics, 25, 15 197–15 243, https://doi.org/10.5194/acp-25-15197-2025, 2025.

Zammit-Mangion, A., Cressie, N., and Ganesan, A. L.: Non-Gaussian bivariate modelling with application to atmospheric trace-gas inversion, Spatial Statistics, 18, 194–220, https://doi.org/10.1016/j.spasta.2016.06.005, 2016.